The American Journal of Pathology, Vol. 193, No. 10, October 2023

ELSEVIER

The American Journal of
PATHOLOGY

ajp.amjpathol.org

MUSCULOSKELETAL PATHOLOGY

Different Mouse Models of Nemaline Myopathy Harboring *Acta1* Mutations Display Differing Abnormalities Related to Mitochondrial Biology

Jennifer A. Tinklenberg,[*†‡] Rebecca A. Slick,[*†‡] Jessica Sutton,[*] Liwen Zhang,[§] Hui Meng,[*] Margaret J. Beatka,[*] Mark Vanden Avond,[*†] Mariah J. Prom,[*] Emily Ott,[*] Federica Montanaro,[¶‖] James Heisner,[†**] Rafael Toro,[††] Edna C. Hardeman,[‡‡] Aron M. Geurts,[†§§] David F. Stowe,[†**¶¶] R. Blake Hill,[††] and Michael W. Lawlor[*†]

From the Division of Pediatric Pathology, Department of Pathology and Laboratory Medicine and Neuroscience Research Center, the Departments of Physiology,† Anesthesiology,** Biochemistry,†† and Biomedical Engineering,¶¶ the Clinical and Translational Science Institute,‡ and the Mellowes Center for Genomic Sciences and Precision Medicine,§§ Medical College of Wisconsin, Milwaukee, Wisconsin; the Mass Spectrometry and Proteomics Facility,§ Campus Chemical Instrument Center, The Ohio State University, Columbus, Ohio; the Dubowitz Neuromuscular Centre,¶ Molecular Neurosciences Section, Developmental Neuroscience Research and Teaching Department, UCL Great Ormond Street Institute of Child Health, London, United Kingdom; the NIHR Great Ormond Street Hospital Biomedical Research Centre,‖ London, United Kingdom; and the School of Medical Sciences,‡‡ University of New South Wales, Sydney, New South Wales, Australia*

Accepted for publication June 23, 2023.

Address correspondence to Michael W. Lawlor, M.D., Ph.D., Medical College of Wisconsin, 8701 W. Watertown Plank Rd., Milwaukee, WI 53226. E-mail: mlawlor@mcw.edu.

ACTA1 encodes skeletal muscle-specific α-actin, which polymerizes to form the thin filament of the sarcomere. Mutations in *ACTA1* are responsible for approximately 30% of nemaline myopathy (NM) cases. Previous studies of weakness in NM have focused on muscle structure and contractility, but genetic issues alone do not explain the phenotypic heterogeneity observed in patients with NM or NM mouse models. To identify additional biological processes related to NM phenotypic severity, proteomic analysis was performed using muscle protein isolates from wild-type mice in comparison to moderately affected knock-in (KI) *Acta1*^{H40Y} and the minimally affected transgenic (Tg) *ACTA1*^{D286G} NM mice. This analysis revealed abnormalities in mitochondrial function and stress-related pathways in both mouse models, supporting an in-depth assessment of mitochondrial biology. Interestingly, evaluating each model in comparison to its wild-type counterpart identified different degrees of mitochondrial abnormality that correlated well with the phenotypic severity of the mouse model. Muscle histology, mitochondrial respiration, electron transport chain function, and mitochondrial transmembrane potential were all normal or minimally affected in the Tg*ACTA1*^{D286G} mouse model. In contrast, the more severely affected KI.*Acta1*^{H40Y} mice displayed significant abnormalities in relation to muscle histology, mitochondrial respirometry, ATP, ADP, and phosphate content, and mitochondrial transmembrane potential. These findings suggest that abnormal energy metabolism is related to symptomatic severity in NM and may constitute a contributor to phenotypic variability and a novel treatment target. *(Am J Pathol 2023, 193: 1548—; https://doi.org/10.1016/j.ajpath.2023.06.008)*

Supported in part by A Foundation Building Strength. The Fusion Orbitrap instrument was supported by NIH grant S10 OD018056. The timsTOF Pro instrument was supported by NIH grant S10 OD026945. F.M. received partial salary support by the NIHR Great Ormond Street Hospital Biomedical Research Centre.

J.A.T. and R.A.S. contributed equally to this work.

Disclosures: M.W.L. is the founder, CEO, and owner of Diverge Translational Science Laboratory. M.W.L. is or has recently been a member of advisory boards for Solid Biosciences, Taysha Gene Therapies, Astellas Gene Therapies (formerly Audentes Therapeutics), and Ichorion Therapeutics. M.W.L. is also a consultant for Astellas Gene Therapies (formerly Audentes Therapeutics), Encoded Therapeutics, Modis Therapeutics, Lacerta Therapeutics, Dynacure, AGADA Biosciences, Affinia Therapeutics, Biomarin, Locanabio, and Vertex Pharmaceuticals. M.W.L. receives research support from Astellas Gene Therapies, Solid Biosciences, Kate Therapeutics, Prothelia, Cure Rare Disease, and Ultragenyx. R.B.H. and R.T. have financial interest in Cytegen, a company developing therapies to improve mitochondrial function. However, neither the research described herein was supported by Cytegen nor was/is in collaboration with the company. All other authors have nothing to disclose.

The views expressed are those of the author(s) and not necessarily those of the National Health Service, the National Institute for Health and Care Research, or the Department of Health.

https://doi.org/10.1016/j.ajpath.2023.06.008

Nemaline myopathy (NM) affects approximately 1 in 50,000[1] children and is linked to pathologic mutations in 14 genes that are mostly related to the sarcomeric thin filament.[2,3] Clinical and pathologic severity varies widely from patient to patient,[4,5] but the presence of distinctive protein aggregates, called nemaline rods, is a characteristic diagnostic feature in patient muscle biopsies. Providing prognostic information to patients with NM is challenging, as there is no clear correlation between symptomatic severity and causative mutation[6] or the degree of nemaline rod pathology.[7]

Mutations in the *ACTA1* gene represent a major cause of NM, as they are responsible for approximately 30% of NM cases.[5] *ACTA1* encodes skeletal muscle-specific α-actin (ACT1A) monomers, which polymerize to form F-actin,[8] the primary structural constituent of the sarcomeric thin filament.[8] Impairment of actin-myosin interactions,[6] improper thin filament construction,[9] and impaired sarcomeric function[10] have all been implicated in muscle weakness due to *ACTA1* mutations but do not fully explain the range of muscle weakness observed in NM.

Mouse models with dominant missense mutations in *Acta1* have been modeled after human mutations, including the knock-in (KI) *Acta1*^{H40Y} mouse[11] and the transgenic (Tg) *ACTA1*^{D286G} mouse.[12] Both mutations cause severe NM in humans, as the patient with the *ACTA1* (D286G) variant died at 9 months of age and the patient with the *ACTA1* (H40Y) variant died at 2 months of age.[13] Mouse models with these mutations display more subtle phenotypes. The KI.*Acta1*^{H40Y} mutation affects the actomyosin interface in approximately 40% of the actin protein,[14] which alters the molecular force production and produces a moderately severe model of NM with significant weakness and spontaneous death in a subset of mice.[11,14,15] In the Tg*ACTA1*^{D286G} mouse model, approximately 20% of the protein is mutated by affecting the actin-actin interface,[12,16] which produces a subtler effect on myosin binding than the KI.*Acta1*^{H40Y} model. The Tg*ACTA1*^{D286G} mice still exhibit mild NM tissue pathology but display minimal weakness on behavioral testing and have a normal lifespan.[12,16,17]

To identify cellular processes that were abnormal across the heterogeneous genetic causes of NM, proteomic analysis of several NM mouse models was performed to identify secondarily affected pathways for further study. In comparing proteomic data sets from the KI.*Acta1*^{H40Y}, Tg*ACTA1*^{D286G}, and nebulin conditional knockout (*Neb* cKO) mice, abnormal protein content related to metabolism was identified to some extent in all models. A comprehensive analysis of the metabolism of *Neb* cKO mice is described elsewhere, and significant findings included severe deficiencies of mitochondrial respiration and ATP content, along with marked abnormalities of mitochondrial distribution and the content and localization of key metabolic regulatory proteins.[18] This report describes the findings of a comprehensive proteomic and metabolic assessment of the Tg*ACTA1*^{D286G} and KI.*Acta1*^{H40Y} mouse models to provide a comparison of metabolic phenotypes in NM. The data support the notion of metabolic dysfunction in NM mice that display significant muscle weakness, which suggests a role for metabolism in contributing to the spectrum of symptomatic severity observed in NM.

Materials and Methods

Live Animal Studies

All studies using animal tissue were approved by the Institutional Animal Care and Use Committee at the Medical College of Wisconsin (Milwaukee, WI). Genotyping was performed as previously described.[19] For all KI.*Acta1*^{H40Y} studies, wild-type (WT; WT.*Acta1*^{H40Y}) and KI (KI.*Acta1*^{H40Y}) littermates were used for comparisons. For all Tg*ACTA1*^{D286G} studies, C57Bl/6J (C57) mice were used as WT control animals because the Tg*ACTA1*^{D286G} was generated by site-directed mutagenesis on CBA × C57Bl/6 mouse embryos to produce the human ACTA1 protein with the D286G mutation.[12]

Assessments were performed at early and late disease stages, as defined below, with the goal of identifying whether specific findings were associated with disease progression. As the goal of proteomics studies was a comparison across models, each model was assessed at the common time points of 6 and 16 weeks of age. As the goal of the histologic and functional testing was the establishment of progression-related phenotypes within a model, different time points were identified for Tg*ACTA1*^{D286G} and KI.*Acta1*^{H40Y} models to reflect their differences in severity and progression. An early disease stage time point corresponded to a time where weakness was present but not severe. For the Tg*ACTA1*^{D286G} mice, 9 weeks of life was selected; and 6 weeks of life was selected for the KI.*Acta1*^{H40Y} as a subpopulation of male KI.*Acta1*^{H40Y} mice die at approximately 6 weeks of life because of complications of bladder outlet obstruction. The late disease stage time point (16 weeks of life for Tg*ACTA1*^{D286G} mice and 9 weeks of life for KI.*Acta1*^{H40Y} mice) corresponded to a time point several weeks later when weakness and pathologic severity were known to have worsened.[15,17] Both male and female mice were used in experiments but because significant differences between sexes were not observed, animals were pooled for statistical analysis.

Tissue Collection

Animals were euthanized using CO_2 and cervical dislocation. Triceps, gastrocnemius, and quadriceps muscles were removed, weighed, and frozen in liquid nitrogen–cooled isopentane.[20]

Table 1 Primary Antibodies and Dilutions Used for Western Blot Analysis and Immunofluorescence Staining

Protein	Antibody	Western blot analysis dilution	Immunofluorescence dilution
NRF2	Abcam (Cambridge, UK) Ab137550	1:750	1:200
KEAP1	Abcam Ab227828	1:1000	1:150
NQO1	Abcam Ab34173	1:1000	1:200
SRF	Abcam Ab53147	1:500	1:75
MRTF-A	Proteintech (Rosemont, IL) 21166-1-AP	1:500	1:200
STARS	Proteintech 22673-1-AP	1:1000	1:200
Vinculin	Cell Signaling (Danvers, MA) 13901S	1:5000	N/A
EIF2S1	Abcam Ab26197	1:500	1:500
ACTN3	Creative Biolabs (Shirley, NY) 9B5	N/A	1:250

ACTN3, alpha-actinin 3; EIF2, eukaryotic translation initiation factor 2; KEAP1, kelch-like ECH-associated protein 1; MRTF-A, myocardin-related transcription factor A; NRF2, nuclear factor erythroid 2–related factor 2; SRF, serum response factor; STARS, striated muscle activator of Rho signaling.

Protein Sample Preparation, Digestion, and Fractionation for Proteomic Analysis

Liquid nitrogen was used to grind frozen quadriceps muscle tissue ($n = 5$ per genotype), and 1 mL of 10% trichloroacetic acid was added per 100 mg tissue in acetone containing 2% mercaptoethanol. This was mixed by inverting the tube 10 times; then, proteins were precipitated overnight at −20°C. Precipitated proteins were centrifuged at 5000 × *g* for 30 minutes at 4°C. They were then washed three times in ice-cold acetone, air dried, and frozen at −80°C until use.

For *Acta1*^{H40Y} early-stage samples (both the mutant and WT), 40 μg of proteins was first separated onto an SDS-PAGE gel based on their different molecular weights and cut into 12 different bands. Gel pieces were then reduced with dithiothreitol and alkylated with iodoacetamide before being in-gel digested by trypsin (sequencing grade; Promega, Madison, WI) at room temperature overnight. After digestion, the peptides were extracted, pooled, and completely dried in a vacufuge, and peptides were resuspended in 20 μL of 50 mmol/L acetic acid for liquid chromatography–tandem mass spectrometry (LC-MS/MS) analysis.

For the rest of three sets of samples, the protein pellets were weighted out and digested with trypsin (protein/enzyme, 100:1) in 50 mmol/L ammonium bicarbonate solution containing 0.1% *Rapi*Gest (Waters Corp., Milford, MA). Samples were reduced with dithiothreitol and alkylated with iodoacetamide before sequencing-grade trypsin was added. Digestion was performed overnight at 37°C. The following day, trifluoroacetic acid was added to a final concentration of 0.5% to the sample and incubated with the samples at 37°C for 30 minutes to precipitate *Rapi*Gest. The sample was then clarified at 15,000 × *g* for 5 minutes in a microcentrifuge, dried in a vacufuge, and resuspended in 40 μL of 50 mmol/L acetic acid. The concentration of the peptides was determined by nanodrop (absorbance 280 nm).

LC-MS/MS Analysis

Peptides obtained from *Acta1*^{H40Y} early-stage and Tg*ACTA1*^{D286G} samples were analyzed on a Thermo Fusion Orbitrap (Thermo Fisher, Coon Rapids, MN) instrument equipped with EASY-Spray Sources operated in positive ion mode. As described previously,[21,22] 1 hour LC gradient and preview mode data-dependent TopSpeed method was used for the analysis after peptide fractionation, either offline or online. *Acta1*^{H40Y} late-stage samples were analyzed on a timsTOF Pro mass spectrometer (Bruker, Eden Prairie, MN) equipped with a CaptiveSpray source operated in positive ion mode using a 2-hour gradient (samples unfractionated). Briefly, samples were separated on a C_{18}

Table 2 Number of Proteins Identified and Differentially Expressed in Each *Acta1* Model at Early and Late Time Points by LC-MS/MS

			$P < 0.05$	
Animal model	Stage	Proteins identified, *N*	Increased >2-fold	Decreased <0.5-fold
KI.*Acta1*^{H40Y}	Early	660	44	15
	Late	1488	115	8
WT.*Acta1*^{H40Y}	Early	624	15	44
	Late	1396	8	115
Tg*ACTA1*^{D286G}	Early	921	33	9
	Late	1076	18	13
C57	Early	897	9	33
	Late	1035	13	18

C57, C57Bl/6J; KI, knock-in; LC-MS/MS, liquid chromatography–tandem mass spectrometry; Tg, transgenic; WT, wild type.

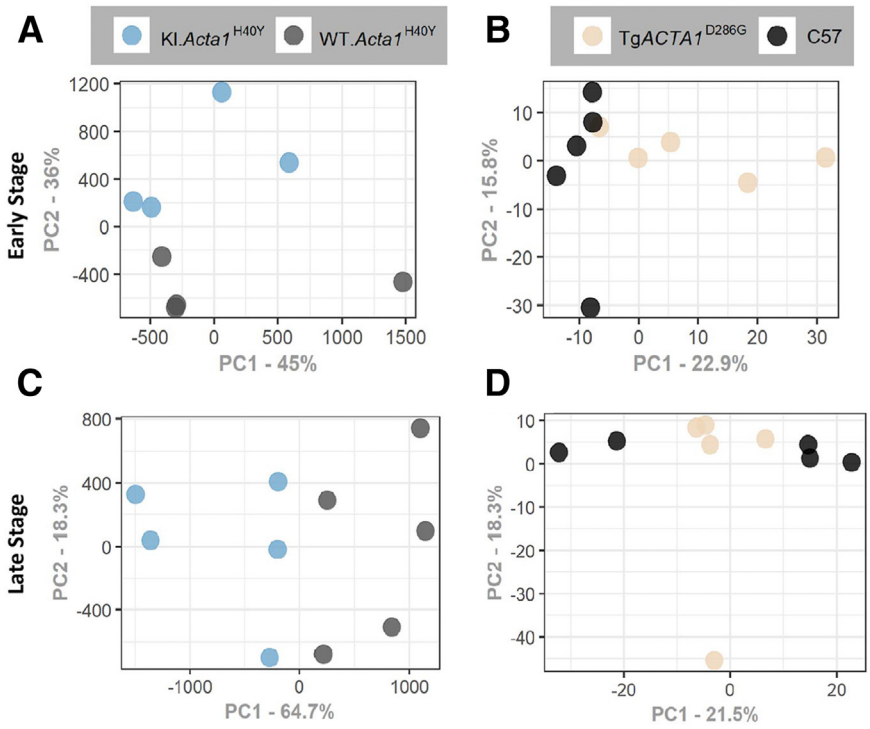

Figure 1 Principal component (PC) analysis of nemaline myopathy mouse models. **A:** Principal component analysis of KI.*Acta1*^{H40Y} early-stage versus wild-type (WT) differential expression data sets. **B:** Principal component analysis of Tg*ACTA1*^{D286G} early-stage versus WT differential expression data sets. **C:** Principal component analysis of KI.*Acta1*^{H40Y} late-stage versus WT differential expression data sets. **D:** Principal component analysis of Tg*ACTA1*^{D286G} late-stage versus WT differential expression data sets.

reverse-phase column (1.6 μm particle size, 250 mm × 75 μm column size; IonOpticks, Fitzroy, VIC, Australia) using a Bruker nanoElute ultra–high-performance LC system. A total of 200 ng desalted peptide was injected for each analysis. Mobile phase A was 0.1% formic acid in water, and acetonitrile (with 0.1% formic acid) was used as mobile phase B. A flow rate of 0.4 μL/minute was used. Mobile phase B was increased from 2% to 17% over the first

Table 3 Top Canonical Pathways Predicted to be Affected in Each Model at Each Stage by IPA

Animal model	Stage	Pathway	*P* value	Overlap
KI.*Acta1*^{H40Y}	Early	Remodeling of epithelial adherens junctions	1.76×10^{-9}	8/69
		Mitochondrial dysfunction	1.30×10^{-8}	10/171
		Cellular effects of sildenafil	1.77×10^{-8}	9/131
		Actin cytoskeletal signaling	2.29×10^{-8}	11/234
		Epithelial adherens junction signaling	6.83×10^{-8}	9/153
	Late	tRNA charging	1.15×10^{-5}	5/39
		Protein ubiquitination pathway	8.09×10^{-5}	10/273
		Sertoli cell–Sertoli cell junction signaling	1.36×10^{-4}	8/185
		Regulation of cellular mechanics by calpain protease	1.83×10^{-4}	5/65
		4-Aminobutyrate degradation I	1.94×10^{-4}	2/3
Tg*ACTA1*^{D286G}	Early	Mitochondrial dysfunction	9.15×10^{-8}	9/171
		Oxidative phosphorylation	6.87×10^{-7}	7/109
		TCA cycle II	4.07×10^{-6}	4/24
		Sirtuin signaling pathway	7.84×10^{-6}	9/292
		Protein ubiquitination pathway	1.54×10^{-3}	6/271
	Late	EIF2 signaling	6.98×10^{-9}	10/232
		Sertoli cell–Sertoli cell junction signaling	4.40×10^{-5}	6/186
		Germ cell–Sertoli cell junction signaling	4.67×10^{-5}	6/188
		Calcium signaling	7.75×10^{-5}	6/206
		Remodeling of epithelial adherens junction	9.43×10^{-5}	4/69

EIF2, eukaryotic translation initiation factor 2; IPA, Ingenuity Pathway Analysis; KI, knock-in; TCA, tricarboxylic acid; Tg, transgenic.

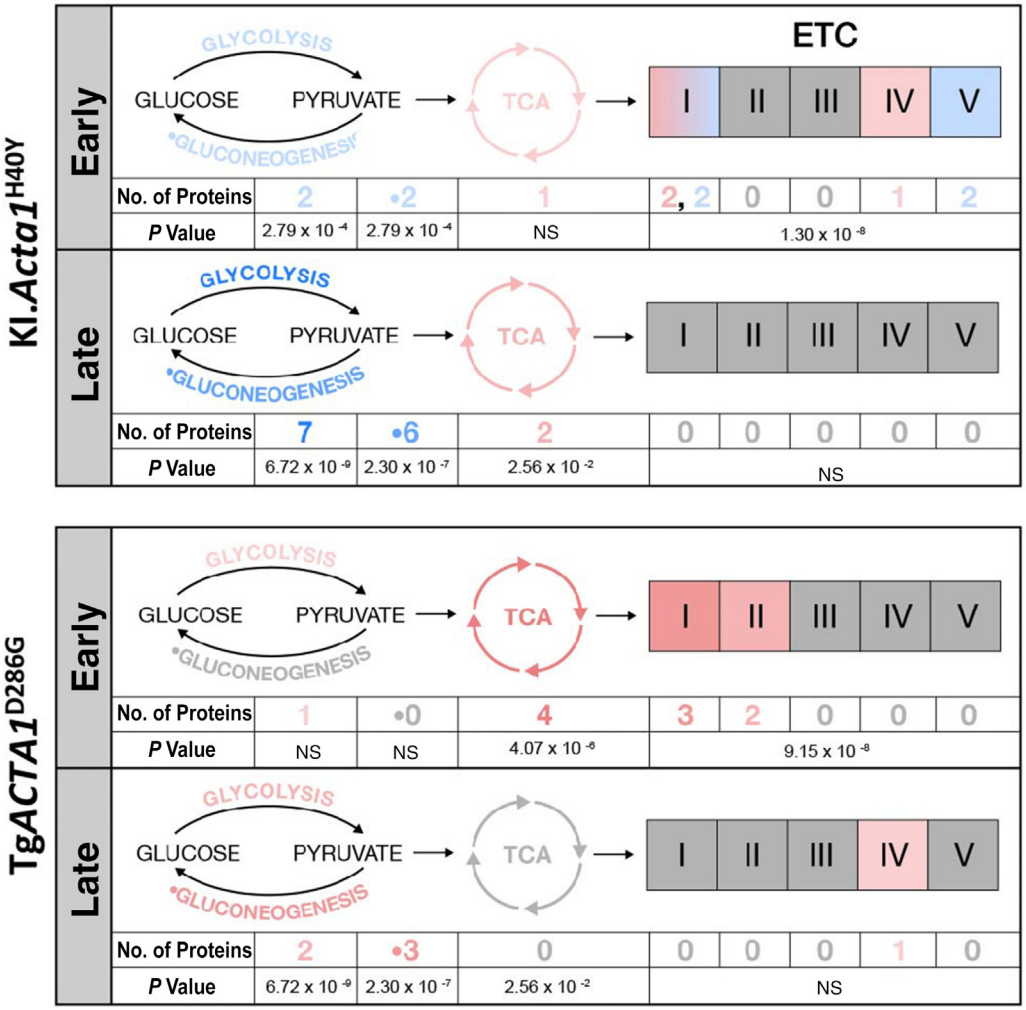

Figure 2 Canonical pathways and protein expression related to energetic metabolism and stress-related pathways are affected differently in each model at each stage. Number of proteins refers to the number of differentially expressed proteins in each data set. Pink represents an increase in expression, whereas blue represents a decrease, with the relative amount of change indicated by the shade of the colors. ETC, electron transport chain; NS, not significant; TCA, tricarboxylic acid.

60 minutes, then increased to 25% over the next 10 minutes, further increased to 37% over the next 10 minutes, and finally increased to 80% over 10 minutes and then held at 80% for 10 minutes. MS and MS/MS experiments were recorded over the *m/z* range 100 to 1700 and the ion mobility range (K_0) of 0.6 to 1.6. Parallel accumulation serial fragmentation (PASEF) was used for all experiments, with the number of PASEF MS/MS scans set to 10. Active exclusion was applied, releasing after 0.4 minutes, with precursor reconsidered if current intensity/previous intensity was $\geq$4.0.

Proteomics Data Analysis and Quantitation

Sequence information from the MS/MS data was then converted into a merged file (mgf) and analyzed using Mascot version 2.6.2 (Matrix Science, Boston, MA). Mascot was set up to search the most recent Uniprot_MOUSE_database. Trypsin was used as the digestion enzyme. Mascot was searched with a fragment ion mass tolerance of 0.50 Da and a parent ion tolerance of 10.0 parts per million. Carbamidomethyl of cysteine was specified in Mascot as a fixed modification. Deamidation of asparagine and glutamine and oxidation of methionine were specified as variable modifications. Scaffold version 5.0.1 (Proteome Software Inc., Portland, OR) was used to validate MS/MS-based peptide and protein identifications. Peptide identifications were accepted if they could be established at >95.0% probability to achieve a false discovery rate of <1.0% by the Peptide Prophet algorithm[23] with Scaffold delta-mass correction. Protein identifications were accepted if they could be established at a false discovery rate of <1.0% and contained at least two identified peptides. Label-free quantitation was performed using the spectral count approach, in which the relative protein quantitation is measured by comparing the number of MS/MS spectra

identified from the same protein in each of the multiple LC-MS/MS data sets.[24] The *t*-test was performed by Scaffold to evaluate if the fold change for certain proteins is significant ($P < 0.05$).

PC Analysis

Principal component (PC) analysis, a dimensionality reduction technique, was used to visualize factors that contribute to each data set's variance. PC analyses were completed in R statistical computing software version 3.5.2 (*https://www.r-project.org*), performed as previously described.[18] Briefly, the prcomp function, which uses singular value decomposition, was applied to each data set. Raw data were visually assessed using scree plots and then plotted using ggplot2.[18] R code used for these analyses is provided in Supplemental Code 1.

Ingenuity Pathway Analysis

The Ingenuity Pathway Analysis (IPA) software package version 84978992 (Qiagen, Germantown, MD) was used to evaluate protein-set enrichment in the KI.*Acta1*^{H40Y} versus WT.*Acta1*^{H40Y} and Tg*ACTA1*^{D286G} versus C57 data sets at early and late time points of disease. For each data set, expression (core) analyses were run using the measurement of expression fold change to calculate directionality z-scores.[18]

Western Blot Analysis

To validate changes in protein content observed in the proteomics data sets, Western blot analyses were performed on quadriceps tissue, as previously described,[18,25] at 16 weeks of age. Polyvinylidene difluoride (PVDF) membranes were probed using antibodies listed in Table 1. Total protein was used for standardization, whereas the remaining targets were used to confirm signals seen in the proteomics dataset. Protein content was quantified using Image Lab Software version 6.1.0 build 7 (Bio-Rad Laboratories, Hercules, CA), and values were normalized to total protein visualized by Ponceau staining or stain-free blot activation. Total protein was used because of difficulty in finding a reliable loading control across all four genotypes.

Muscle Immunofluorescence

Frozen quadriceps samples were sectioned transversely at 8 μm, and three tissue sections were mounted per slide. Tissue sections were stained with primary antibodies listed in Table 1 at 16 weeks of age to validate the proteomics data sets. Secondary antibodies include the following: goat anti-rabbit IgG Alexa Fluor 594 (Invitrogen, Waltham, MA; A11012, 1:400) and goat anti-mouse IgG1 Alexa Fluor 488 (Invitrogen; A21121; 1:400). Images were captured using a Leica SP8 Upright Confocal Microscope (Leica Microsystems, Buffalo Grove, IL).

Histologic Evaluation

Immunohistochemistry was performed on the triceps of five male and five female mice of each genotype at 9 weeks of life. Hematoxylin and eosin, Gömöri trichrome, or cytochrome oxidase (COX) stains were performed using standard techniques on cross-sections (8 μm thick) mounted onto glass slides. Images were taken using a Leica DFC 7000T camera with Leica LAS X software version 3.5.2 mounted to a Leica DMB6 B microscope (Leica Microsystems). Images of each stain were taken at ×200 magnification so that each image contained between 138 and 204 total muscle fibers for five animals of each genotype. Matching areas between stains were used to quantify the number of total cells, cells with aggregates on Gömöri trichrome, and cells with mitochondrial abnormalities on COX using ImageJ software version 1.53e (NIH, Bethesda, MD: *http://imagej.nih.gov/ij*, last accessed February 10, 2023).[26] In addition, the COX and Gömöri trichrome stains were compared to count how many of the cells with aggregates on the Gömöri trichrome stain overlapped with aggregates or mislocalized mitochondria on the COX stain. Cell counts of each abnormality were then converted to a percentage of the total fibers of each image field. Electron microscopy was performed, as previously described,[18] and submitted to the Electron Microscopy Core Facility at the Medical College of Wisconsin. Epoxy resin-embedded tissues were cut and imaged on a Hitachi H600 transmission electron microscope (Hitachi, Tokyo, Japan) equipped with an Advanced Microscopy Techniques (AMT; Woburn, MA) digital imaging system with special focus on mitochondrial ultrastructure for each sample.

Mitochondrial Isolation from Muscle Tissue

Mitochondria were isolated from skeletal muscle of both male and female mice using a standard protocol,[27] with the modifications previously described.[18] For both time points of the C57 and Tg*ACTA1*^{D286G} as well as the 9-week KI.*Acta1*^{H40Y} and WT.*Acta1*^{H40Y}, each sample corresponded to mitochondria from a single animal. However, the tissue for two animals needed to be pooled for each sample at the 6-week KI.*Acta1*^{H40Y} time point to get appropriate protein concentrations for analysis. These isolates were used for mitochondrial respirometry, electron transport chain (ETC) function, and mitochondrial transmembrane potential ($\Delta\Psi_m$).

Respiratory Control Index

A Clark Oxygen Electrode (model S 200A; Strathkelvin Instruments, Glasgow, Scotland) was used to measure oxygen consumption of the respiring mitochondria, as previously

Table 4 Pathways Downstream of NRF2 Activation Are Predicted to be Affected to Different Degrees Across Models and Time Points

Mouse model and stage	NRF2-mediated stress response		Glutathione redox reactions		Thioredoxin reductase reactions	
	P value	Proteins changed, *N*	*P* value	Proteins changed, *N*	*P* value	Proteins changed, *N*
KI.*Acta1*^{H40Y} ES	5.57×10^{-4}	4 Up, 2 down	6.20×10^{-3}	2 Up	NS	0
KI.*Acta1*^{H40Y} LS	NS	0	NS	0	NS	0
Tg*ACTA1*^{D286G} ES	NS	0	1.82×10^{-2}	1 Up	NS	0
Tg*ACTA1*^{D286G} LS	5.80×10^{-3}	3 Up, 1 down	3.07×10^{-3}	2 Up	NS	0

(*table continues*)

ES, early stage; KI, knock-in; LS, late stage; NRF2, nuclear factor erythroid 2—related factor 2; NS, not significant; redox, oxidation-reduction; Tg, transgenic.

described.[18] Isolated skeletal muscle mitochondria use glutamate/malate and ADP to respire as they consume oxygen and convert it into ATP and water. The decrease in the oxygen content of the chamber can then be used to calculate the respiratory control index (RCI) of the mitochondrial sample.

ETC Enzyme Functional Assays

Assays for all ETC complexes were performed on mitochondrial isolates per the manufacturers' instructions, with minor modifications at both early and late time points. Assay details are summarized in Supplemental Table S1 and described in detail in the study by Slick et al.[18] Bovine heart mitochondria were used as a quality control to ensure the assay worked as intended and activity buffers were working correctly. In each assay, the colorimetric change over time is proportional to the enzyme activity. Any sample with a concentration of <5.5 mg/mL or any assay that had a failed bovine heart mitochondria curve was excluded from the data set.

ATP, ADP, and Phosphate Assays

One triceps from each mouse was used to perform ATP (Abcam, Cambridge, UK; ab83355), ADP (ab83359), and phosphate (ab65622) assays, per the manufacturer's instructions at the animals' early time points only. Assays are outlined in Supplemental Table S2 and described in more detail in the study by Slick et al.[18] Briefly, triceps were minced and homogenized in their appropriate buffer and centrifuged to remove cellular debris. The amount of supernatant used in each assay was adjusted per sample to ensure the sample reading fell within one of the two standard curves. Concentrations of ATP, ADP, or phosphate were calculated on the basis of the standard curve, calculated per μL of sample, and the results were then normalized to the average protein concentration.

Mitochondrial Transmembrane Potential

Mitochondrial isolations, as described above at early time points, were used for the analysis of $\Delta\Psi_m$ using the Mitochondria Staining Kit (Sigma, St. Louis, MO; CS0760) per the manufacturer's instructions and as previously described.[18] For all samples, 5 μg of protein was loaded per well. The red fluorescence of the JC-1 (5,5′,6,6′-tetrachloro1,1′,3,3′-tetraethylbenzimidazolocarbocyanine iodide) aggregates was measured at excitation/emission 490 nm/590 nm and 485 nm/535 nm for the JC-1 monomer green fluorescence.[28] Mitochondrial transmembrane potential was then determined by the ratio of red/green fluorescence after a 20-minute incubation.

Statistical Analysis

Statistical analysis was performed using Prism 9.1.2 software (GraphPad, Inc., La Jolla, CA). A two-way analysis of variance was used to analyze age and genotype differences in cell counts, RCI, and ETC analyses. The Tukey multiple comparisons test was used for two-way analysis of variance post tests. Unpaired *t*-tests were used to compare protein expression of pathway proteins, ATP, ADP, phosphate, and $\Delta\Psi_m$ between mutant and WT animals. Data are presented as the means ± SEM, with significance set to $P < 0.05$ for all experiments.

Results

Differential Expression Analysis and Data Visualization

Although different LC-MS/MS platforms were used for some of the analysis, typical muscle proteins, such as myosin, α-actinin, actin, tropomyosin, myotilin, γ-filamin, cofilin-2, and telethonin, were identified across all samples. A comparison between each *Acta1* model and its WT counterpart suggested that the level of these proteins between mutant and WT groups remained mostly unchanged no matter which platform was used for sample analysis. Differentially expressed proteins were defined by a fold change of <0.5 or >2. The mass spectrometry proteomics data have been deposited to the ProteomeXchange Consortium via the PRIDE[29] partner repository, with the data set identifier PXD042201.

Table 4 (*continued*)

Xenobiotic metabolism signaling		NAD(P)H repair		Heme degradation		Iron homeostasis signaling	
P value	Proteins changed, *N*	*P* value	Proteins changed, *N*	*P* value	Proteins changed, *N*	*P* value	Proteins changed, *N*
NS	0	1.47×10^{-2}	1 Up	NS	0	6.11×10^{-5}	1 Up
NS	0	3.09×10^{-2}	1 Down	4.10×10^{-2}	1 Up	NS	0
NS	0	1.37×10^{-2}	1 Up	NS	0	2.50×10^{-2}	3 Up
3.92×10^{-3}	3 Up, 2 down	NS	0	NS	0	NS	0

At the early stage, 660 proteins were identified in the KI.*Acta1*^{H40Y}, whereas 624 proteins were identified in the WT.*Acta1*^{H40Y} group (Table 2 and Figure 1A). Of these, 44 proteins significantly increased and 15 significantly decreased in the KI.*Acta1*^{H40Y} group compared with the WT group (Table 2, Figure 1A, Supplemental Figure S1A, and Supplemental Table S3). At late stage, 1488 total proteins were identified in the KI.*Acta1*^{H40Y} and 1396 proteins were identified in the WT.*Acta1*^{H40Y} mice, with 115 significantly increased and 8 significantly decreased in the KI.*Acta1*^{H40Y} animals compared with those in WT (Table 2, Figure 1A, Supplemental Figure S1C, and Supplemental Table S4).

In the Tg*ACTA1*^{D286G} mouse model, 921 proteins were identified at early stage and 1076 were identified at late stage, with 897 and 1035 proteins being identified in the C57 data sets, respectively (Table 2, Figure 1A, and Supplemental Tables S5 and S6). At early stage, 33 proteins were determined to be increased and 9 were decreased in the

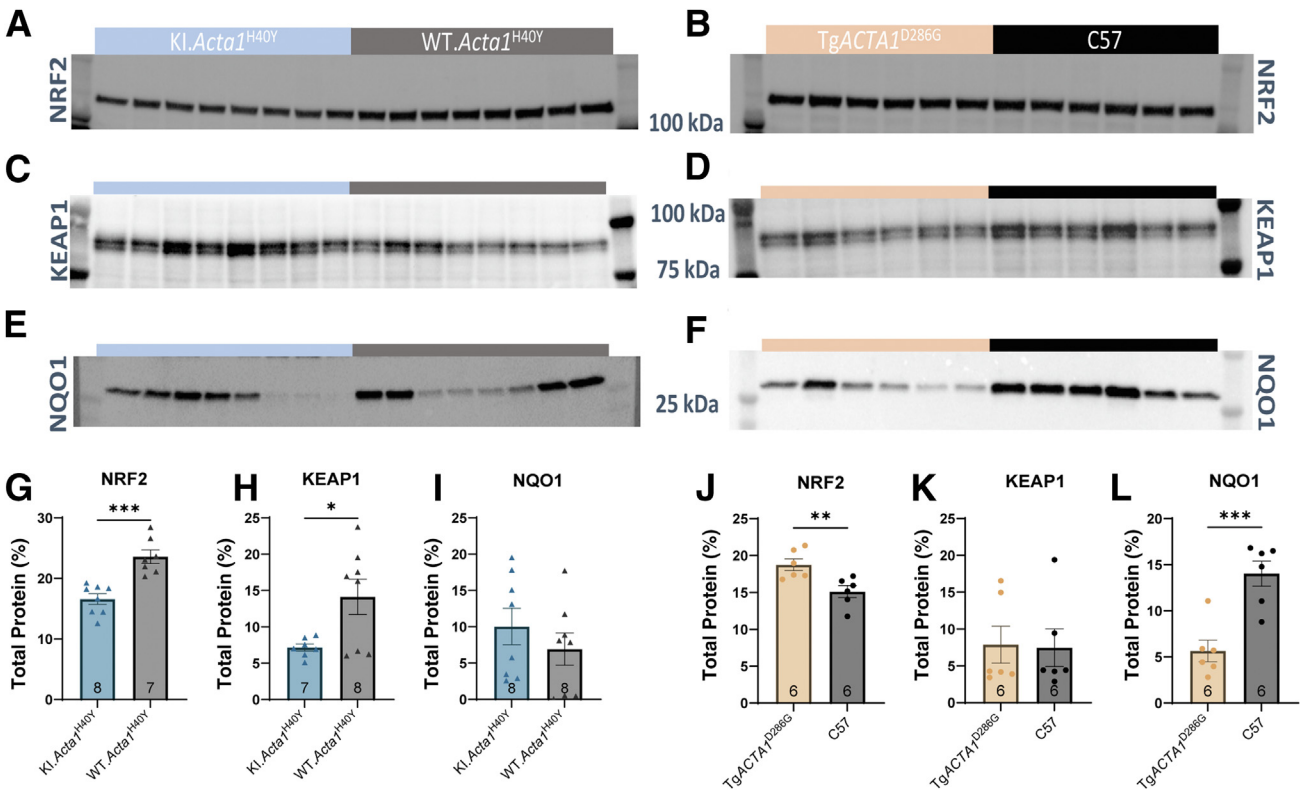

Figure 3 Nuclear factor erythroid 2–related factor 2 (NRF2) pathway protein expression is differentially affected in two *Acta1* nemaline myopathy models. **A** and **G:** NRF2 expression is decreased between KI.*Acta1*^{H40Y} and wild-type (WT) animals at late stage. **B** and **J:** NRF2 expression is significantly increased in the Tg*ACTA1*^{D286G} animals versus their WT counterparts at late stage ($P = 0.009$). **C**, **D**, **H**, and **K:** Kelch-like ECH-associated protein 1 (KEAP1) expression is decreased in the KI.*Acta1*^{H40Y} animals and not changed in the Tg*ACTA1*^{D286G} animals at late stage. **E** and **I:** NAD(P)H dehydrogenase [quinone] 1 (NQO1) protein expression is not different in the KI.*Acta1*^{H40Y} animals versus their WT counterparts at late stage. **F** and **L:** NQO1 expression is significantly decreased in the Tg*ACTA1*^{D286G} animals at late stage. $^{*}P < 0.05$, $^{**}P < 0.01$, and $^{***}P < 0.001$. C57, C57Bl/6J.

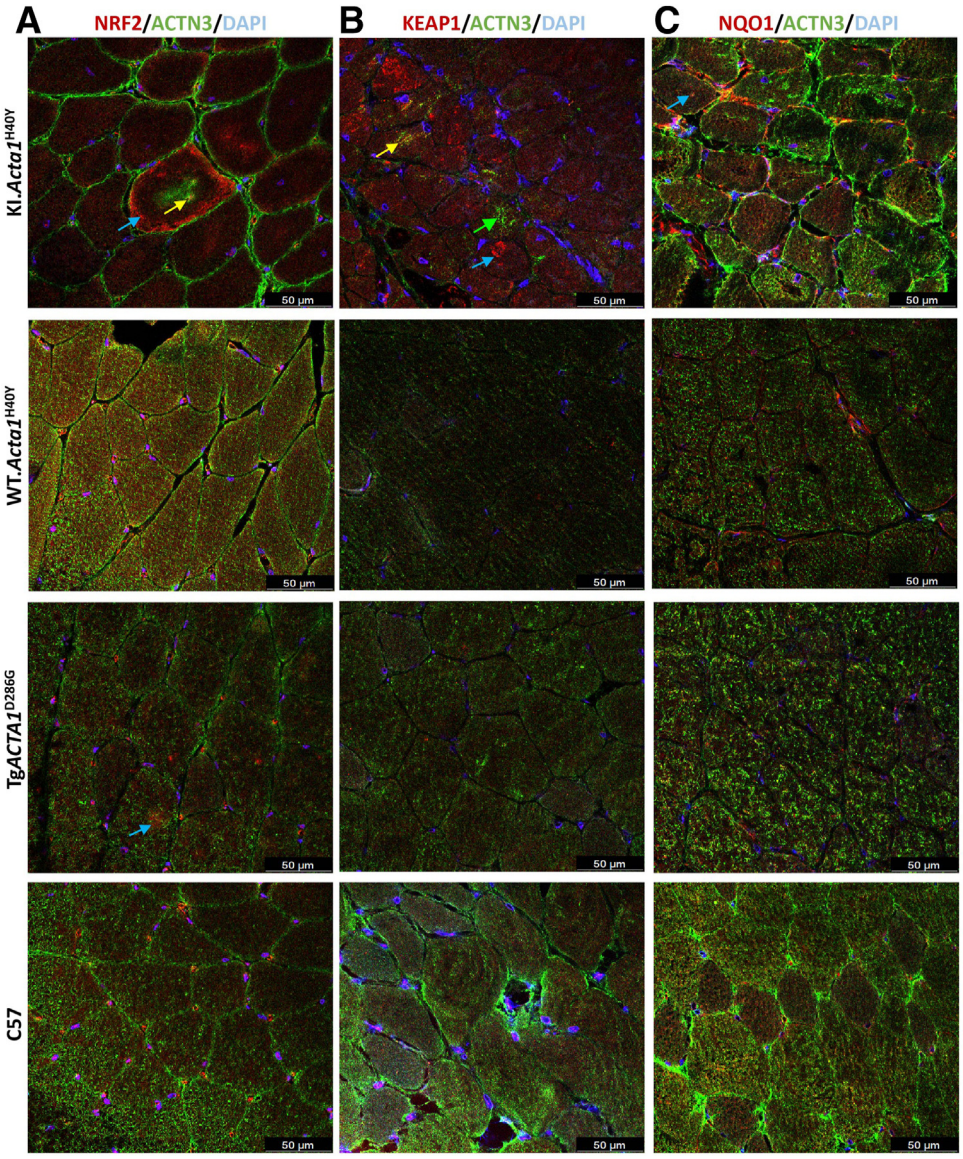

Figure 4 Nuclear factor erythroid 2–related factor 2 (NRF2) pathway protein localization is differentially affected in two *Acta1* nemaline myopathy models. **A:** NRF2 is localized to aggregates separate to nemaline rods in the KI.*Acta1*^{H40Y} and Tg*ACTA1*^{D286G} animals at late stage. **B:** Kelch-like ECH-associated protein 1 (KEAP1) is mislocalized to cytoplasmic aggregates in the KI.*Acta1*^{H40Y} animals but has normal localization in the Tg*ACTA1*^{D286G} animals at late stage. **C:** NAD(P)H dehydrogenase [quinone] 1 (NQO1) localizes to cytoplasmic aggregates and nemaline rods in the KI.*Acta1*^{H40Y} animals at late stage. NQO1 localization is not altered in the Tg*ACTA1*^{D286G} animals at late stage. (**Blue arrows** indicate cytoplasmic aggregates; **green arrows**, nemaline rods; and **yellow arrows**, co-localization with nemaline rods.) Scale bars = 50 μm (**A**–**C**). ACTN3, alpha-actinin 3.

Tg*ACTA1*^{D286G} animals (Table 2, Figure 1A, and Supplemental Figure S1B), whereas 18 proteins were increased and 13 were decreased in late-stage animals (Table 2, Figure 1A, and Supplemental Figure S1D).

Principal component analysis of each individual data set was run using R (Supplemental Table S7). In the early-stage KI.*Acta1*^{H40Y} mouse muscle, PC1 contributed to 45% of variability, whereas PC2 contributed to 36% of variability, within the data set (Figure 1A). PC2 separated the KI.*Acta1*^{H40Y} animals from their WT counterparts; and based on an Enrichr analysis, the top 20 proteins in PC2 were related to striated muscle contraction, computational model of aerobic glycolysis, Cori cycle, hypoxia inducible factor 1 subunit alpha (HIF1A) and peroxisome proliferator activated receptor gamma (PPARG) regulation of glycolysis and gluconeogenesis, and urea cycle and metabolism of amino groups (Supplemental Table S8). At late stage, PC1 accounted for 64.7% variability and separated the KI.*Acta1*^{H40Y} animals from their WT counterparts (Figure 1C). The top 20 proteins in PC1 were involved in similar pathways as at early stage based on Enrichr analysis (Supplemental Table S9).

At early stage in the Tg*ACTA1*^{D286G} animals, PC1 accounted for 22.9% of variability within the data set,

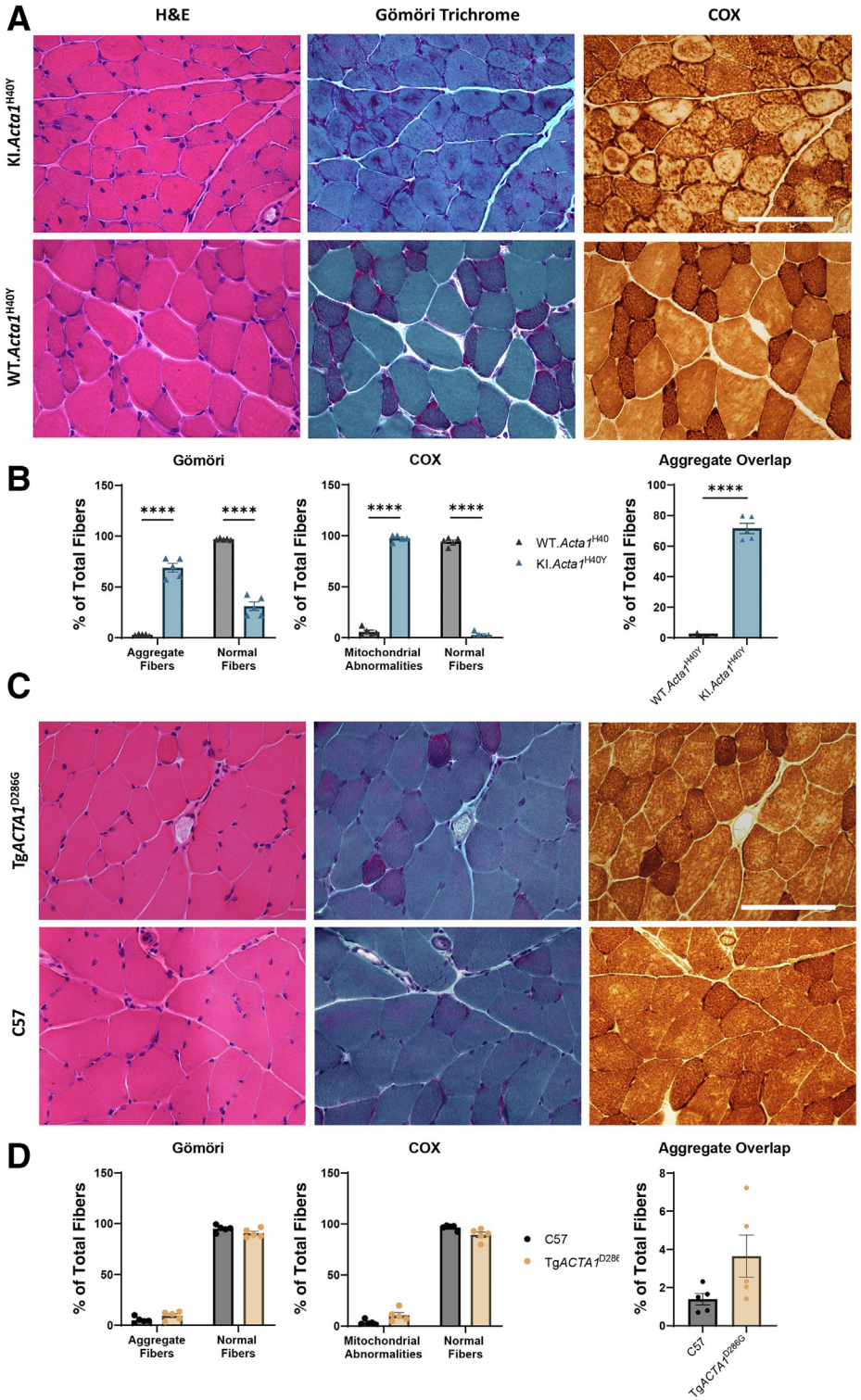

Figure 5 Structural differences are seen in the *Acta1* mouse models of nemaline myopathy. **A:** KI.*Acta1*^{H40Y} animals had smaller muscle fibers on hematoxylin and eosin (H&E) stain and significant aggregation on Gömöri trichrome stain. KI.*Acta1*^{H40Y} animals also had a unique staining pattern on cytochrome oxidase (COX) that highlights both mitochondrial aggregates as well as areas where mitochondria appear nearly absent. **B:** KI.*Acta1*^{H40Y} animals had a significant number of cells with aggregates on Gömöri trichrome stain and a significant number of cells with abnormal mitochondria compared with wild-type (WT) animals. There was also significant overlap in the cells with aggregates on the Gömöri trichrome stain with cells that had abnormal mitochondria on the COX stain, indicating that some aggregates seen on the Gömöri stain were not nemaline rods, but mitochondrial aggregates. **C:** Tg*ACTA1*^{D286G} animals had minimal muscle pathology on H&E, Gömöri trichrome, or COX stains compared with WT animals. **D:** Tg*ACTA1*^{D286G} animals did not have significant increases in the number of cells with aggregates on the Gömöri trichrome stain or cells with mitochondrial abnormalities with the COX stain. There was also no significant overlap of aggregate cells with mitochondrial abnormalities. ****$P < 0.0001$. Scale bar = 100 μm (**A** and **C**). Original magnification, ×400 (**A** and **C**). C57, C57Bl/6J.

Table 5 Percentage of Total Fibers with Aggregates and Nonuniform Mitochondrial Distribution in the KI.*Acta1*^{H40Y} Mouse

	WT.*Acta1*^{H40Y}		KI.*Acta1*^{H40Y}		
Variable	% of Total fibers	SEM	% of Total fibers	SEM	*P* value
Fibers with aggregates	2.99	0.37	68.95	4.22	<0.0001
Nonuniform mitochondrial distribution	5.84	1.76	97.48	1.32	<0.0001
Overlap	1.33	0.55	71.6	3.38	<0.0001

KI, knock-in; WT, wild type.

whereas PC2 contributed to 15.8% of variability (Figure 1B). PC1 appeared to separate the Tg*ACTA1*^{D286G} animals from their WT counterparts. The top 20 proteins that contributed to PC1 were analyzed by Enrichr related to WikiPathway 2021, including ketogenesis and ketolysis, γ-glutamyl cycle for the biosynthesis and degradation of glutathione, methionine metabolism, leading to sulfur amino acids and related disorders, nucleotide metabolism, glutathione metabolism, lipid metabolism pathway, fatty acid β-oxidation, and energy metabolism (Supplemental Table S10). In the Tg*ACTA1*^{D286G} mice at late stage, PC1 and PC2 accounted for 21.5% and 18.3% of variability, respectively. Neither PC1 nor PC2 separated the late stage Tg*ACTA1*^{D286G} mice from their WT counterpart (Figure 1D). Overall, it appears that a large amount of variability between diseased mice and their WT counterparts could be accounted for by proteins involved in pathways related to striated muscle contraction and energy metabolism.

Pathways Predicted to Be Affected by IPA

After preliminary data visualization and analysis, the differential expression data sets were run through IPA individually using $P = 0.05$ and fold change cutoff values of 1.5 and −1.5 to identify pathways and networks predicted to be perturbed on the basis of changes in protein content. The top five canonical pathways for each data set are shown in Table 3 and Figure 2 and largely relate to energetic metabolism, tRNA charging, eukaryotic translation initiation factor 2 (EIF2) signaling, and actin-related signaling. Calcium signaling and protein ubiquitination pathways were also predicted to be affected, but as they were less consistently present, metabolic- and stress-related pathways were further evaluated to identify secondary processes that contribute to NM pathogenesis.

Because of the prediction that energetic metabolism is affected in *Acta1*-NM, protein content related to the IPA canonical pathways glycolysis, gluconeogenesis, tricarboxylic acid cycle, and each ETC complex was further assessed. In the KI.*Acta1*^{H40Y} mice, protein levels related to glycolysis and gluconeogenesis were decreased, whereas protein levels related to the tricarboxylic acid cycle were increased, at both stages (Figure 2). At early stage, protein expression of molecules known to be part of ETC complexes I, IV, and V was abnormal (Figure 2). At early stage in the Tg*ACTA1*^{D286G} mice, protein content related to glycolysis, the tricarboxylic acid cycle, and ETC complexes I and II was increased (Figure 2); and proteins related to glycolysis, gluconeogenesis, and ETC complex IV increased at late stage (Figure 2).

Pathway Validation

Pathways identified to be relevant based on proteomic and bioinformatic screening of global protein content signatures were further evaluated to determine if the changes in protein content seen in the proteomics were relevant in the mouse tissue itself. Western blots were used to quantify changes in protein content, whereas immunofluorescence (IF) was used to determine whether localization of key pathway proteins was altered with or without significant changes in protein content. The late-stage time point of 16 weeks was used for all pathway validations as changes in protein expression or localization as progression-related accumulations or mislocalizations of protein are more likely to be apparent at late stage.

Table 6 Percentage of Total Fibers with Aggregates and Nonuniform Mitochondrial Distribution in the Tg*ACTA1*^{D86G} Mouse

	C57		Tg*Acta1*^{D286G}		
Variable	% of Total fibers	SEM	% of Total fibers	SEM	*P* value
Fibers with aggregates	4.92	1.49	9.40	1.88	NS
Nonuniform mitochondrial distribution	3.44	1.07	10.54	2.64	NS
Overlap	1.39	0.30	3.64	1.11	NS

C57, C57Bl/6J; NS, not significant; Tg, transgenic.

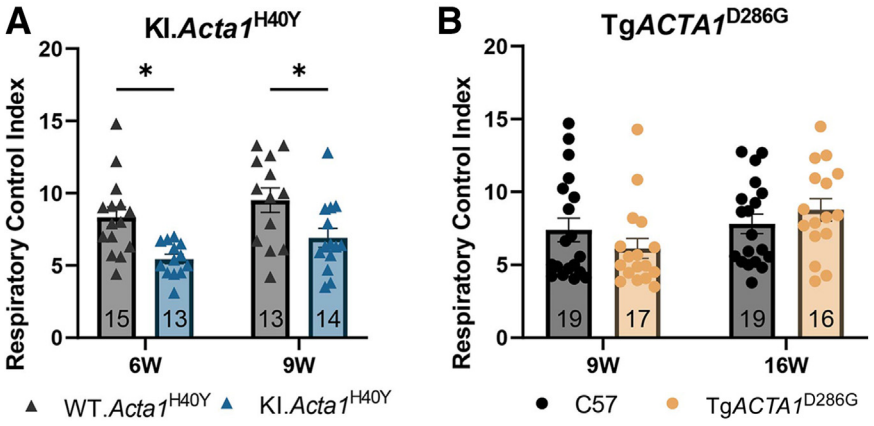

Figure 6 Mitochondrial respirometry in *Acta1* mice. **A:** KI.*Acta1*^{H40Y} mice had a significant reduction in respiratory control index at both 6 and 9 weeks when compared with wild-type (WT) littermates. **B:** Tg*ACTA1*^{D286G} mice had no significant differences in mitochondrial respirometry at either 9 or 16 weeks when compared with C57Bl/6J (C57) animals. *$P < 0.05$.

Nuclear Factor Erythroid 2–Related Factor 2

Nuclear factor erythroid 2–related factor 2 (NRF2), an upstream regulator by IPA, was predicted to be activated in the KI.*Acta1*^{H40Y} mice at early and late stages, and potentially affected in the early-stage Tg*ACTA1*^{D286G} mice. Downstream effects of NRF2 activation were evaluated by analyzing IPA pathways affected by NRF2 activation. Canonical pathways, including the NRF2-mediated stress response, glutathione oxidation-reduction reactions, thioredoxin reductase reactions, xenobiotic metabolism signaling, NAD(P)H repair, heme degradation, and iron homeostasis signaling, were analyzed in IPA; and changes in protein content are noted in Table 4 and Figure 3A. Similar to metabolic pathways, a variety of pathways downstream of NRF2 activation were predicted to be affected to varying degrees across all four data sets, most notably in KI.*Acta1*^{H40Y} at early stage and in Tg*ACTA1*^{D286G} at late stage (Table 4 and Figure 3A).

To confirm changes in protein content seen in the proteomics data sets and evaluate localization of these proteins, Western blot and IF of NRF2-related proteins were performed using late-stage KI.*Acta1*^{H40Y} and Tg*ACTA1*^{D286G} animals and respective WT mice. The upstream regulator (NRF2), its inhibitory regulator kelch-like ECH-associated protein 1 (KEAP1), and a downstream transcriptional target NAD(P)H dehydrogenase [quinone] 1 (NQO1) were investigated. NRF2 and KEAP1 were significantly decreased, whereas NQO1 protein expression was not different in KI.*Acta1*^{H40Y} compared with WT.*Acta1*^{H40Y} tissue (Figure 3, A, C, E, and G–I). The localization of all three proteins, however, was abnormal, as IF for these markers identified cytoplasmic aggregates or colocalization with nemaline rods as indicated by alpha-actinin 3 (ACTN3) in KI.*Acta1*^{H40Y} muscle (Figure 4). Skeletal muscle from Tg*ACTA1*^{D286G} mice displayed an increase in NRF2 protein content, no change in KEAP1, and a decrease in NQO1 compared with muscle from C57 control mice (Figure 3, B, D, F, and J–L). NRF2 localized to cytoplasmic aggregates separate from nemaline rods in a small amount of myofibers in Tg*ACTA1*^{D286G} muscle, whereas KEAP1 had a potential increase in perinuclear localization and NQO1 had localization similar to C57 samples (Figure 4). Collectively, these data confirm that proteins related to NRF2 pathway activation are abnormal in protein content and/or localization in the Tg*ACTA1*^{D286G} and KI.*Acta1*^{H40Y} animals and confirm the proteomic data set's indication that the NRF2 pathway is differently affected across *Acta1*-NM models.

Serum Response Factor

It was postulated that NM mutations could affect pathways that respond to structural changes of the thin filament because of predicted changes in actin-related processes by IPA. The serum response factor (SRF) pathway is an important pathway in skeletal muscle that is known to regulate >200 genes related to skeletal muscle growth, function, cytoskeletal structure, metabolism, and regeneration.[30] In NM, Z-disk proteins are mislocalized, which may stimulate striated muscle activator of Rho signaling (STARS) activation and promote SRF pathway activity. Therefore, protein content and localization of SRF, STARS, myocardin-related transcription factor A (MRTF-A), and vinculin were analyzed by Western blot and/or IF.

SRF and vinculin levels were significantly greater in the KI.*Acta1*^{H40Y} than in WT.*Acta1*^{H40Y} tissue, whereas there was no difference in STARS or MRTF-A expression

Table 7 RCI for the KI.*Acta1*^{H40Y} Mouse

Animal model	RCI	SEM
WT.*Acta1*^{H40Y}		
6 Weeks	8.35	0.69
9 Weeks	9.51	0.85
KI.*Acta1*^{H40Y}		
6 Weeks	5.45	0.32
9 Weeks	6.91	0.66

KI, knock-in; RCI, respiratory control index; WT, wild type.

Table 8 RCI for the Tg*ACTA1*^{D86G} Mouse

Animal model	RCI	SEM
C57		
9 Weeks	7.40	0.81
16 Weeks	7.81	0.66
Tg*ACTA1*^{D286G}		
9 Weeks	6.12	0.69
16 Weeks	8.77	0.77

C57, C57Bl/6J; RCI, respiratory control index; Tg, transgenic.

between them (Supplemental Figure S2, A, C, E, G, and I–L). In KI.*Acta1*^{H40Y} samples, SRF appeared to have an increase in nuclear content, suggesting increased activation (Supplemental Figure S3A). STARS and MRTF-A were mislocalized to cytoplasmic aggregates in the KI.*Acta1*^{H40Y} mice (Supplemental Figure S3, B and C). In Tg*ACTA1*^{D286G} tissue, SRF content was significantly decreased, whereas STARS, MRTF-A, and vinculin were unchanged compared with C57 samples (Supplemental Figure S2, B, D, F, H, and M–P). STARS and MRTF-A had normal localization in Tg*ACTA1*^{D286G} cross-sections compared with WT mice (Supplemental Figure S3, B and C). Overall, changes in SRF pathway protein content or localization substantiate the proteomic data and indicate a role of SRF pathway proteins in NM pathophysiology.

Eukaryotic Translation Initiation Factor 2

The EIF2 signaling pathway was determined to be of interest as it was predicted to be an affected canonical pathway in both NM models and at both late and early disease stages. In addition, the EIF2 signaling pathway was the top canonical pathway to be affected in the late-stage Tg*ACTA1*^{D286G} animals. tRNA charging, which relates to EIF2 activation, was the top canonical pathway predicted to be affected in the late-stage KI.*Acta1*^{H40Y} animals (Table 3). The IPA canonical pathway EIF2 signaling was predicted to be affected in the early- and late-stage KI.*Acta1*^{H40Y} animals and early-stage Tg*ACTA1*^{D286G} animals ($P = 2 \times 10^{-5}$, 3.59×10^{-2}, and 2.19×10^{-2}, respectively) and predicted to be activated in the late-stage Tg*ACTA1*^{D286G} animals ($P = 6.98 \times 10^{-9}$; z-score = 2.449). When uncharged tRNAs accumulate, they act upstream to activate EIF2.[31] The canonical pathway tRNA charging was not indicated in the early-stage KI.*Acta1*^{H40Y} or either of the Tg*ACTA1*^{D286G} data sets but was predicted to be activated in the late-stage KI.*Acta1*^{H40Y} animals ($P = 1.51 \times 10^{-5}$; z-score = 2.236).

An increase in EIF2 content or nuclear localization would indicate activation and validate the proteomics data sets. By Western blot analysis, the KI.*Acta1*^{H40Y} animals had no change in total EIF2 content compared with their WT counterparts (Supplemental Figure S4, A and C). However, by IF, the KI.*Acta1*^{H40Y} mice appeared to have increased nuclear localization and some punctate cytoplasmic localization compared with WT.*Acta1*^{H40Y} mice (Supplemental Figure S4E). Similarly, the Tg*ACTA1*^{D286G} mice had no change in EIF2 protein content (Supplemental Figure S4, B and D) but had a potential increase in nuclear localization of EIF2 in comparison to C57 mice, suggesting an increase in activation (Supplemental Figure S4E). Phosphorylated EIF2 was also probed in an attempt to quantify the amount of active EIF2, but the results were not interpretable. Therefore, further experiments are necessary to truly determine the relevance of the EIF2 pathway in *Acta1*-NM.

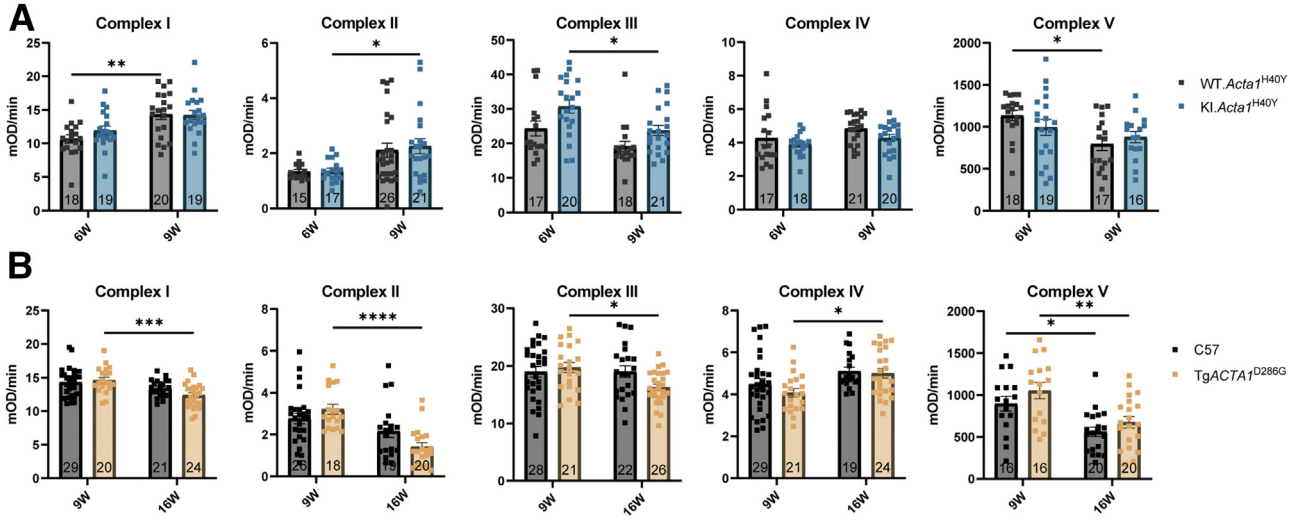

Figure 7 Electron transport chain (ETC) enzyme activity assays in *Acta1* mice. Both KI.*Acta1*^{H40Y} (**A**) and Tg*ACTA1*^{D286G} (**B**) animals had no significant differences in enzyme function in any complexes of the ETC between wild-type (WT) and mutant animals. However, significant differences were seen between ages of animals within each enzyme. *$P < 0.05$, **$P < 0.01$, ***$P < 0.001$, and ****$P < 0.0001$. C57, C57Bl/6J; mOD, milli-optical density.

Table 9 Average Enzyme Activity for Each Enzyme of the Electron Transport Chain in the KI.*Acta1*^{H40Y} Mouse

	Complex I			Complex II			Complex III			Complex IV			Complex V		
Animal model	mOD/minute	SEM	*P* value	mOD/minute	SEM	*P* value	mOD/minute	SEM	*P* value	mOD/minute	SEM	*P* value	mOD/minute	SEM	*P* value
WT.*Acta1*^{H40Y}			<0.01			NS			NS			NS			<0.05
6 Weeks	10.7	0.6		1.33	0.07		24.35	2.13		4.27	0.39		1133.71	60.53	
9 Weeks	14.35	0.76		2.11	0.25		19.11	1.49		4.84	0.19		796.34	78.59	
KI.*Acta1*^{H40Y}			NS			<0.05			<0.05			NS			NS
6 Weeks	11.93	0.65		1.36	0.1		30.7	1.89		3.88	0.16		992.34	95.11	
9 Weeks	14.25	0.69		2.26	0.27		23.8	1.47		4.28	0.22		876.92	65.75	

KI, knock-in; mOD, milli-optical density; NS, not significant; WT, wild type.

Mitochondrial Aggregation and Mislocalization Are Seen in NM Mouse Muscle

Histologic evaluation was performed using sections (8 μm thick) of isopentane-frozen triceps muscle at 6 (Supplemental Figure S5A) and 9 (Figure 5A) weeks of life.[20] The KI.*Acta1*^{H40Y} mice had significant pathology by hematoxylin and eosin, Gömöri trichrome, and COX stains. As previously described, pathologic findings included small fibers and internal nucleation on hematoxylin and eosin stain[11,15] as well as significant aggregation on the Gömöri trichrome stain (Figure 5A), with no observable fiber type abnormalities.[15,17] The COX stain also had a unique pattern of mitochondrial mislocalization in the KI.*Acta1*^{H40Y} animals, with nearly every fiber showing mitochondrial aggregation, areas devoid of mitochondria, or a combination of both (Figure 5A). In addition, double staining with COX and succinate dehydrogenase (SDH) was performed and showed identical staining patterns to the COX stain alone (data not shown). This staining was performed to evaluate for COX-negative fibers that can be associated with mitochondrial dysfunction in muscle biopsies, although this abnormality is much more commonly observed in adult mitochondrial disease rather than pediatric mitochondrial disease. The aggregates seen on the Gömöri trichrome stain had a significant overlap with the aggregation seen on the COX stain, indicating that at least some of the pathologic aggregates correspond to collections of both nemaline rods and mitochondrial aggregates (Figure 5B and Table 5). These findings were further illustrated at the ultrastructural level by the presence of collections of nemaline rods, myofibrillar disarray, and abnormalities of mitochondria that included enlargement, focal clustering of mitochondria, and other areas of myofibers that appeared to be devoid of mitochondria in the intermyofibrillar space in KI.*Acta1*^{H40Y} animals compared with their WT counterparts (Supplemental Figure S6).

Triceps muscle tissue from Tg*ACTA1*^{D286G} mice had minimal pathology at both 9 (Figure 5C) and 16 (Supplemental Figure S5B) weeks of life, indicative of nemaline myopathy, as previously described.[17] Myofibers appeared appropriately sized on hematoxylin and eosin stain and had few areas of aggregated red material on the Gömöri trichrome stain (Figure 5, C and D, and Table 6). Similarly, the stain for complex IV of the ETC using COX had few fibers with mitochondrial mislocalization (Figure 5, C and D). There was no significant overlap between the population of myofibers with aggregates of red material on Gömöri trichrome stain in comparison to mislocalized mitochondria on COX stain (Figure 5D). Electron microscopy sections on Tg*ACTA1*^{D286G} animals indicated rare nemaline rods, but mitochondrial placement, number, and morphology were normal in comparison to C57 animals (Supplemental Figure S6).

Table 10 Average Enzyme Activity for Each Enzyme of the Electron Transport Chain in the Tg*ACTA1*^{D86G} Mouse

	Complex I			Complex II			Complex III			Complex IV			Complex V		
Animal model	mOD/minute	SEM	*P* value	mOD/minute	SEM	*P* value	mOD/minute	SEM	*P* value	mOD/minute	SEM	*P* value	mOD/minute	SEM	*P* value
C57			NS			NS			NS			NS			<0.05
9 Weeks	14.32	0.39		2.77	0.25		19.01	0.89		4.49	0.26		897.37	87.75	
16 Weeks	13.44	0.28		2.17	0.25		19.02	1.01		5.11	0.19		561.98	56.73	
Tg*ACTA1*^{D286G}			<0.001			<0.0001			<0.05			<0.05			<0.01
9 Weeks	14.62	0.43		3.21	0.24		19.73	0.88		4.07	0.2		1052.95	95.82	
16 Weeks	12.38	0.38		1.42	0.2		16.26	0.57		5.01	0.23		675.73	68.61	

C57, C57Bl/6J; mOD, milli-optical density; NS, not significant; Tg, transgenic.

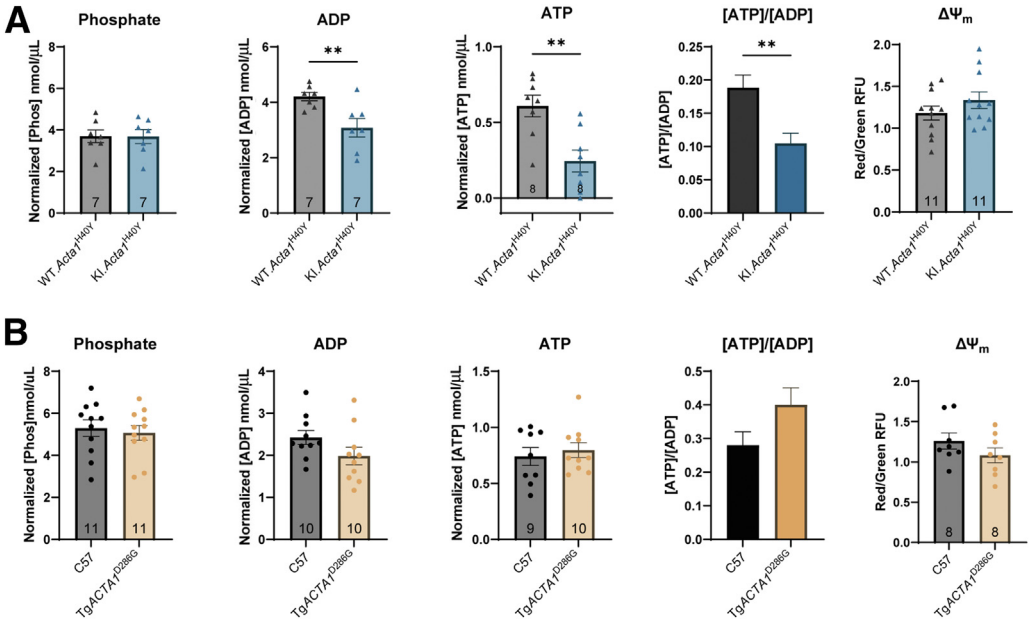

Figure 8 Changes in phosphate, ADP, ATP, and membrane potential in *Acta1* mice. **A:** KI.*Acta1*^{H40Y} animals had significant decreases in the amount of ATP and ADP, but not phosphate or mitochondrial transmembrane potential ($\Delta\Psi_m$). **B:** Tg*ACTA1*^{D286G} animals had no significant changes to phosphate, ADP, or ATP levels in tissue isolates or any changes in $\Delta\Psi_m$. Phosphate, ADP, and ATP samples were normalized to protein concentration. $^{**}P < 0.01$.

Mitochondrial Assays

Mitochondrial Respirometry

Isolated mitochondria were used to investigate mitochondrial respiratory function by calculating the RCI to evaluate the overall health of the mitochondria. The KI.*Acta1*^{H40Y} animals had significant decreases to RCI values at both 6 (WT.*Acta1*^{H40Y} versus KI.*Acta1*^{H40Y}: 8.35 ± 0.69 versus 5.45 ± 0.32; $P = 0.0154$) and 9 (WT.*Acta1*^{H40Y} versus KI.*Acta1*^{H40Y}: 9.51 ± 0.85 versus 6.91 ± 0.66; $P = 0.0406$) (Figure 6A and Table 7) weeks of life, indicating impaired mitochondrial function.[32] However, the Tg*ACTA1*^{D286G} animals did not have significant changes in RCI values when compared with C57 animals at either 9 (C57 versus Tg*ACTA1*^{D286G}: 7.40 ± 0.81 versus 6.12 ± 0.69; $P = 0.610$) or 16 (C57 versus Tg*ACTA1*^{D286G}: 7.81 ± 0.66 versus 8.77 ± 0.77; $P = 0.802$) (Figure 6B and Table 8) weeks of life.

Evaluation of ETC and Its Constituents

Each enzyme of the ETC was examined for total enzyme activity. For each assay, the change in OD over time was analyzed in the most linear portions of the graphs. Data and specific statistical comparisons are provided in Figure 7 and summarized in Tables 9 and 10. Briefly, significant changes were seen between ages within genotypes in all complexes with the exclusion of the *Acta1*^{H40Y} animals' complex IV (Figure 7). The KI.*Acta1*^{H40Y} animals did not have significant differences between genotypes in any of the five complexes at 6 or 9 weeks (Figure 7A). In addition, no significant changes were seen in any complex activity in Tg*ACTA1*^{D286G} animals compared with C57 animals at 9 or 16 weeks (Figure 7B). Significant differences to various degrees were observed between ages of the same genotype in both groups of animals (Figure 7).

The amount of ATP, ADP, and phosphate was analyzed only at the early time points for each genotype set and is summarized in Tables 11 and 12. The more severe KI.*Acta1*^{H40Y} animals had significant changes in the amount of ATP (WT.*Acta1*^{H40Y} versus KI.*Acta1*^{H40Y}: 0.61 ± 0.07 versus 0.24 ± 0.07 normalized [ATP] nmol/μL; $P = 0.003$), ADP (WT.*Acta1*^{H40Y} versus KI.*Acta1*^{H40Y}: 4.20 ± 0.15 versus 3.08 ± 0.33 normalized [ADP] nmol/μL; $P = 0.010$), and the [ATP]/[ADP] ratio (WT.*Acta1*^{H40Y} versus KI.*Acta1*^{H40Y}: 0.19 ± 0.01 versus 0.10 ± 0.02 [ATP]/[ADP]; $P = 0.005$), but not in the amount of phosphate present (Figure 8A). The Tg*ACTA1*^{D286G} animals had no changes in the amount of ATP, ADP, ratio of [ATP]/[ADP], or phosphate (Figure 8B) in tissue isolates in comparison to isolates from C57 animals. However, even with these significant changes in ATP levels in the KI.*Acta1*^{H40Y} mice, neither *Acta1*-NM animal models had significant changes in their $\Delta\Psi_m$ compared with their respective WT animals (Figure 8).

Discussion

In searching for secondary disease processes that may contribute to disease severity in NM, proteomic analysis indicated changes in cellular stress pathways and mitochondrial biology in all assessed animal models. The current

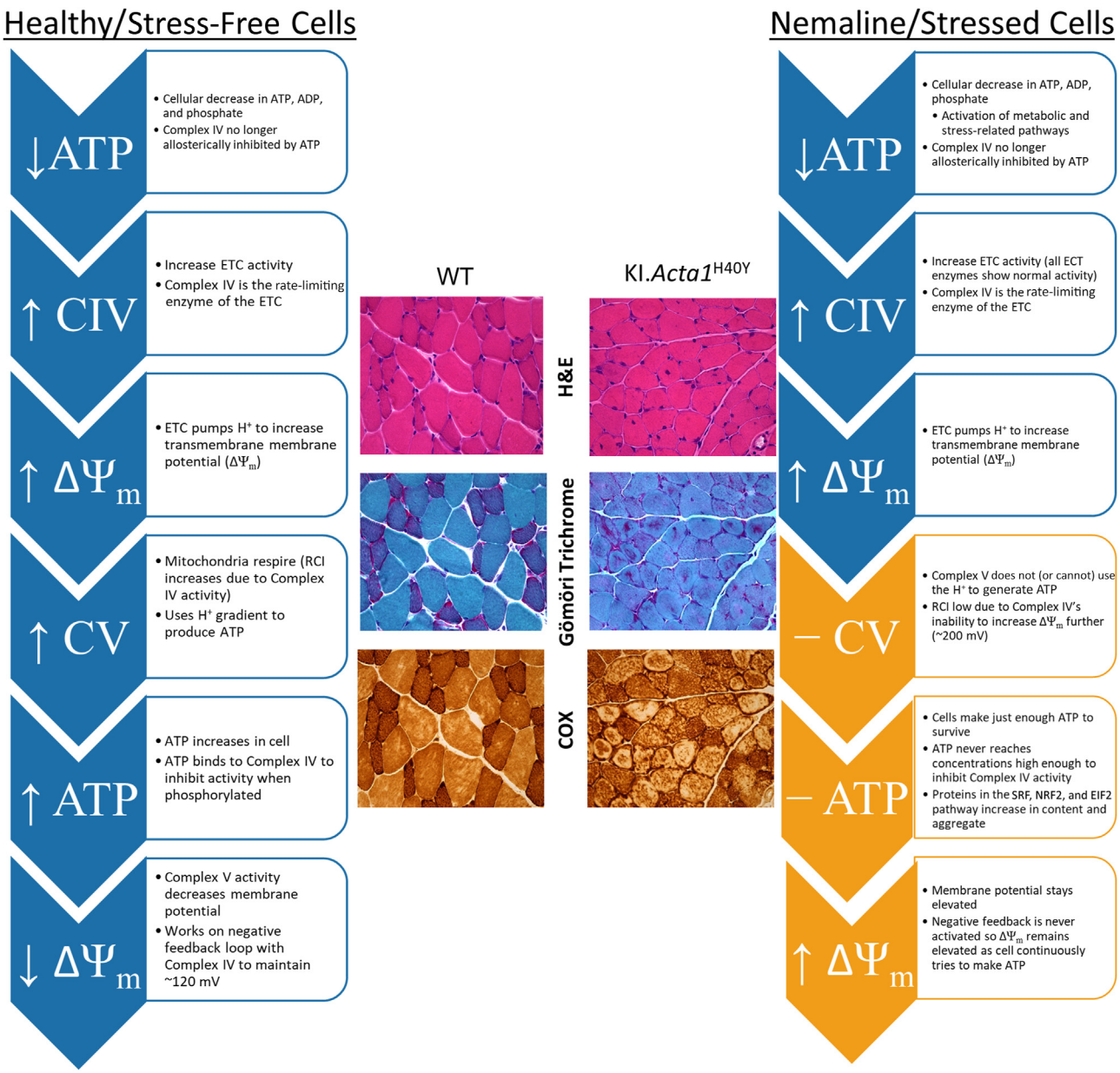

Figure 9 Working model of changes in nemaline myopathy (NM) mouse metabolism and stress pathways. Changes in protein expression and stress pathways impact muscle morphology and mitochondrial homeostasis in NM mouse models. $\Delta\Psi_m$, mitochondrial transmembrane potential; CIV, complex IV; COX, cytochrome oxidase; CV, complex V; EIF2, eukaryotic translation initiation factor 2; ETC, electron transport chain; H&E, hematoxylin and eosin; NRF2, nuclear factor erythroid 2–related factor 2; RCI, respiratory control index; SRF, serum response factor.

study provides assessments of signaling pathways, mitochondrial distribution, and mitochondrial function in Tg*ACTA1*^{D286G} and KI.*Acta1*^{H40Y} mice in comparison to WT counterparts. Each of these *Acta1* point mutations affected the actin protein structure and function differently and presumably altered cellular stress and energy metabolism disparately in each model. Functional and structural analyses confirmed the presence of significant abnormalities in all assessed areas in the KI.*Acta1*^{H40Y} mice, but not Tg*ACTA1*^{D286G} mice. These findings suggest that mitochondrial biology is a relevant biological process for study in NM but is not uniformly present in all NM models.

Previous studies in the laboratory performed comprehensive phenotypic assessments of both mouse models.[15,17] The Tg*ACTA1*^{D286G} animals showed a significant decrease in body mass and individual muscle weight, a decrease in grip strength, and a decrease in voluntary running wheel activity compared with C57 animals.[17] Compared with WT.*Acta1*^{H40Y}, the KI.*Acta1*^{H40Y} animals also showed significant decreases in animal mass and individual muscle

Table 11 Average Values for Total Phosphate, ADP, ATP, [ATP]/[ADP] Ratio, and $\Delta\Psi_m$ in the KI.*Acta1*^{H40Y} Mouse

	Phosphate			ADP			ATP			[ATP]/[ADP] ratio			$\Delta\Psi_m$		
Animal model	Normalized [phosphate], nmol/μL	SEM	*P* value	Normalized [ADP], nmol/μL	SEM	*P* value	Normalized [ATP], nmol/μL	SEM	*P* value	Normalized [ATP]/[ADP] ratio, nmol/μL	SEM	*P* value	Red/green RFU	SEM	*P* value
WT.*Acta1*^{H40Y}			NS			<0.01			<0.01			<0.01			NS
6 Weeks	3.69	0.31		4.20	0.15		0.61	0.07		0.19	0.01		1.18	0.08	
KI.*Acta1*^{H40Y}															
6 Weeks	3.68	0.33		3.08	0.33		0.24	0.07		0.1	0.02		1.34	0.10	

$\Delta\Psi_m$, mitochondrial transmembrane potential; KI, knock-in; NS, not significant; RFU, relative fluorescence units; WT, wild type.

weights as well as grip strength and a reduced life span.[15] Although these two *Acta1* animal models were not directly compared, the KI.*Acta1*^{H40Y} animals had a more severe phenotype than the Tg*ACTA1*^{D286G} animals, although they have the same altered gene. This indicates the importance of investigating secondary processes outside of the primary genetic mutation to help explain the variability of muscle weakness seen in NM.

It is possible that metabolic- and stress-related pathways are activated in NM because of two things. First, sarcomeric disorganization likely induces activation of these pathways to compensate for structural changes, which contribute to increased $\Delta\Psi_m$ in a severity-dependent manner. Second, decreased levels due to the inability to produce ATP, or the increased ATP cost of basal metabolism in NM,[33] likely further activate metabolic- and stress-related pathways. These processes generate a feed-forward effect that alters protein content, leading to protein aggregation and alterations in ATP synthesis, ultimately leading to a decrease in available energy, which, in turn, adds more cellular stress (Figure 9).

A bioinformatic-to-pathway validation approach was used to elucidate important processes and identify potential biomarkers in NM.[18] Although protein expression data showed that the change in protein amount does not necessarily equal the degree of protein activation or function, especially in a disease of protein aggregation. Here, the NRF2, SRF, and EIF2 pathways were determined to be relevant across two *Acta1*-NM models of varying severity at late stage using the same approach as with the *Neb* cKO mice.

NRF2, SRF, and EIF2 were not detected by mass spectrometry in any *Acta1* data sets, but downstream protein content signatures point to these pathways being altered in some capacity in both *Acta1* mouse models. In general, an increase in protein content and mislocalization to cytoplasmic aggregates were associated with more severe disease (Table 13). All interrogated proteins were mislocalized in the KI.*Acta1*^{H40Y} model, whereas only NRF2 was mislocalized in the Tg*ACTA1*^{D286G} mice. Most notably, in the more severe KI.*Acta1*^{H40Y} model, proteins related to the NRF2 and SRF pathways appeared to mislocalize to cytoplasmic aggregates and/or nuclei to a greater extent than in the Tg*ACTA1*^{D286G} mice (Table 13). Because of differences in protein isolation methods, nemaline rods and other protein aggregates were likely not captured in Western blot experiments.

Regardless, even in a mild disease state, the NRF2 pathway appeared to be altered, with NRF2 being localized to cytoplasmic aggregates with or without a change in protein content in Tg*ACTA1*^{D286G} and KI.*Acta1*^{H40Y} muscle tissue (Table 13). The KI.*Acta1*^{H40Y} animals had decreased protein levels of key NRF2 pathway proteins, including

Table 12 Average Values for Total Phosphate, ADP, ATP, [ATP]/[ADP] Ratio, and $\Delta\Psi_m$ in the Tg*ACTA1*^{D86G} Mouse

	Phosphate			ADP			ATP			[ATP]/[ADP] ratio			$\Delta\Psi_m$		
Animal model	Normalized [phosphate], nmol/μL	SEM	*P* value	Normalized [ADP], nmol/μL	SEM	*P* value	Normalized [ATP], nmol/μL	SEM	*P* value	Normalized [ATP]/[ADP] ratio, nmol/μL	SEM	*P* value	Red/green RFU	SEM	*P* value
C57			NS			NS			NS			NS			NS
9 Weeks	5.30	0.39		2.43	0.17		0.74	0.08		0.28	0.03		1.26	0.01	
Tg*ACTA1*^{D286G}															
9 Weeks	5.07	0.35		2.00	0.21		0.58	0.07		0.40	0.05		1.08	0.09	

$\Delta\Psi_m$, mitochondrial transmembrane potential; C57, C57Bl/6J; NS, not significant; RFU, relative fluorescence units; Tg, transgenic.

Table 13 EIF2, NRF2, and SRF Pathway Proteins Are Altered in Expression and/or Localization to Varying Degrees across Three Mouse Models of NM

Pathway	Protein	WB analysis or IF	Tg*ACTA1*^{D286G} (mild)	KI.*Acta1*^{H40Y} (moderate)	*Neb* cKO (severe)
EIF2	EIF2	WB analysis	No change	No change	Decreased
		IF	Possible increase in nuclear localization	Possible increase in nuclear localization, some samples with punctate cytoplasmic localization	Abnormal cytoplasmic localization
	pEIF2	WB analysis	N/A	N/A	Increased
NRF2	NRF2	WB analysis	Increased	Decreased	Increased
		IF	Abnormal localization to aggregates	Abnormal localization to aggregates greater than Tg*ACTA1*^{D286G}	Abnormal localization to aggregates in a greater number of fibers than KI.*Acta1*^{H40Y}
	KEAP1	WB analysis	No change	Decreased	Increased
		IF	No change	Localization to cytoplasmic aggregates	Localization to cytoplasmic aggregates in more fibers and with greater intensity than the KI.*Acta1*^{H40Y}; some colocalization with nemaline rods
	NQO1	WB analysis	Decreased	No change	Increased
		IF	No change	Localization to cytoplasmic aggregates; some colocalization with nemaline rods	Localization to cytoplasmic aggregates in more fibers and with greater intensity than the KI.*Acta1*^{H40Y}; some colocalization with nemaline rods
SRF	SRF	WB analysis	Decreased	Increased	Increased
		IF	No change	Increased nuclear localization	N/A
	STARS	WB analysis	No change	No change	N/A
		IF	No change	Localization to cytoplasmic aggregates	N/A
	MRTF-A	WB analysis	No change	No change	No change
		IF	No change	Localization to cytoplasmic aggregates, colocalization to nemaline rods	Localization to cytoplasmic aggregates in more fibers and with greater intensity than KI.*Acta1*^{H40Y} muscle; some colocalization with nemaline rods
	Vinculin	WB analysis	No change	Increased	Increased

EIF2, eukaryotic translation initiation factor 2; IF, immunofluorescence; KEAP1, kelch-like ECH-associated protein 1; MRTF-A, myocardin-related transcription factor A; N/A, not applicable; *Neb* cKO, nebulin conditional knockout; NM, nemaline myopathy; NQO1, NAD(P)H dehydrogenase [quinone] 1; NRF2, nuclear factor erythroid 2–related factor 2; pEIF2, phosphorylated EIF2; STARS, striated muscle activator of Rho signaling; WB, Western blot.

NRF2 and KEAP1, with no changes to NQO1. All three proteins were mislocalized to cytoplasmic aggregates, including and separate from nemaline rods in KI.*Acta1*^{H40Y} tissue. The Tg*ACTA1*^{D286G} animals had a significant increase in NRF2 protein content, no change in KEAP1, and a significant decrease in NQO1. Under healthy conditions, an increase in NRF2 content would be indicative of NRF2 activation and lead to an increase in downstream protein expression of proteins, including NQO1.[34] The increase in NRF2 content but decrease in NQO1 content in the Tg*ACTA1*^{D286G} animals suggests abnormal functioning of NRF2. In further support of this idea, NRF2 was mislocalized in Tg*ACTA1*^{D286G} quadriceps sections and localized to aggregates, including and separate from nemaline rods. Localization of other key NRF2 pathway proteins was not affected in the Tg*ACTA1*^{D286G} animals. More importantly, mislocalization and aggregation of proteins in the NRF2 pathway appeared to increase with disease severity as the KI.*Acta1*^{H40Y} samples had increased NRF2, KEAP1, and NQO1 mislocalization in comparison to the Tg*ACTA1*^{D286G} samples (Table 13).

The three mouse models examined for changes in the NRF2, SRF, and EIF2 pathways are summarized in Table 13. An investigation of the *Neb* cKO mouse showed that proteins related to the NRF2, SRF, and EIF2 pathways were altered in content, localization, or both, to varying degrees in muscle tissue correlated with a more severe disease phenotype (Table 13).[18] With the exception of NRF2 and KEAP1, changes in protein expression were altered in a disease severity-dependent manner. Changes in KEAP1 localization to protein aggregates increased with disease severity. The Tg*ACTA1*^{D286G} animals showed no changes in expression or localization, whereas the KI.*Acta1*^{H40Y} animals showed no changes in expression but exhibited changes in localization. Lastly, the most severe model, the *Neb* cKO, showed both an increase in protein

expression as well as altered protein localization. In addition, the Tg*ACTA1*^{D286G}, mild disease, showed decreases in NQO1 and SRF protein content on Western blot analysis; however, increases in protein content were associated with the increased disease severity of the KI.*Acta1*^{H40Y} and *Neb* cKO (Table 13). This indicated an increase in activation of these cellular stress pathways with increase in disease severity; however, whether these changes are causative or compensatory as protein expression increases remains unclear as more of the proteins get sequestered in aggregates.

Mitochondrial function has been implicated as a variable that constitutes a cause and a consequence of muscle weakness in NM. A possible relationship between mitochondrial function and disease severity in NM has been alluded to, as the mildly symptomatic Tg*ACTA1*^{D286G} mice showed little to no perturbations of mitochondrial biology, whereas moderate abnormalities of mitochondrial biology were observed in the moderately symptomatic KI.*Acta1*^{H40Y} mouse model. Interestingly, more severe mitochondrial issues were identified in the severely symptomatic *Neb* cKO model of NM.[18] These findings suggest that mitochondrial biology is a relevant biological process contributing to NM, as there may be a relationship between mitochondrial biology and symptomatic severity in NM.

Changes in mitochondrial function are seen in the more severe KI.*Acta1*^{H40Y} animals, but not the Tg*ACTA1*^{D286G} animals. These changes in mitochondrial respiration are not caused by changes in ETC function or an altered $\Delta\Psi_m$. The levels of phosphate, ATP, ADP, and the ratio of [ATP]/[ADP] are not changed in the Tg*ACTA1*^{D286G} animals but are more negatively impacted in the more severe KI.*Acta1*^{H40Y} animals. These data combined with pathway validation assessments suggest that stress-related mitochondrial signaling abnormalities may need to exceed a certain threshold of protein expression or signaling abnormality before disease-related changes impact mitochondrial function.

The pattern of mitochondrial functional abnormality detected in KI.*Acta1*^{H40Y} mice was similar to what was described in the *Neb* cKO mouse model of NM.[18] Interestingly, the *Neb* cKO mice displayed the most severe structural and mitochondrial functional abnormalities of the three NM models tested, and also had the most severe behavioral phenotype. *Neb* cKO muscle had severe functional abnormalities of mitochondrial respiration, ATP and ADP concentrations, and $\Delta\Psi_m$. Similar abnormalities were detected in the same assays when testing muscle from KI.*Acta1*^{H40Y} mice, although the degree of abnormality in comparison to controls was less pronounced. As the KI.*Acta1*^{H40Y} mice are much less severely affected than *Neb* cKO mice, and these assays were not significantly abnormal in the Tg*ACTA1*^{D286G} model (which has minimal behavioral abnormalities). There was an association between the degree of symptomatic severity in these mouse models and the degree of mitochondrial functional abnormality.

Whether the mitochondrial dysfunction contributes to muscle weakness observed in these models, is a downstream consequence of NM muscle weakness, or both, is unclear. The relationship between contractile deficiency, energy metabolism, and metabolic dysfunction is an area of active investigation as new assays and cellular models of NM continue to be developed for testing. Overall, the findings suggest that mitochondrial dysfunction in NM may contribute to the severity of the disease phenotypes, which may provide a novel treatment target that would be effective independent of causative mutation.

Supplemental Data

Supplemental material for this article can be found at *http://doi.org/10.1016/j.ajpath.2023.06.008*.

References

1. North KN, Laing NG, Wallgren-Pettersson C: Nemaline myopathy: current concepts: the ENMC international consortium and nemaline myopathy. J Med Genet 1997, 34:705−713
2. Sewry CA, Laitila JM, Wallgren-Pettersson C: Nemaline myopathies: a current view. J Muscle Res Cell Motil 2019, 40:111−126
3. Nilipour Y, Nafissi S, Tjust AE, Ravenscroft G, Hossein Nejad Nedai H, Taylor RL, Varasteh V, Pedrosa Domellof F, Zangi M, Tonekaboni SH, Olive M, Kiiski K, Sagath L, Davis MR, Laing NG, Tajsharghi H: Ryanodine receptor type 3 (RYR3) as a novel gene associated with a myopathy with nemaline bodies. Eur J Neurol 2018, 25:841−847
4. Ryan MM, Ilkovski B, Strickland CD, Schnell C, Sanoudou D, Midgett C, Houston R, Muirhead D, Dennett X, Shield LK, De Girolami U, Iannaccone ST, Laing NG, North KN, Beggs AH: Clinical course correlates poorly with muscle pathology in nemaline myopathy. Neurology 2003, 60:665−673
5. Agrawal PB, Strickland CD, Midgett C, Morales A, Newburger DE, Poulos MA, Tomczak KK, Ryan MM, Iannaccone ST, Crawford TO, Laing NG, Beggs AH: Heterogeneity of nemaline myopathy cases with skeletal muscle alpha-actin gene mutations. Ann Neurol 2004, 56:86−96
6. Feng JJ, Marston S: Genotype-phenotype correlations in ACTA1 mutations that cause congenital myopathies. Neuromuscul Disord 2009, 19:6−16
7. Malfatti E, Romero NB: Nemaline myopathies: state of the art. Rev Neurol (Paris) 2016, 172:614−619
8. Sparrow JC, Nowak KJ, Durling HJ, Beggs AH, Wallgren-Pettersson C, Romero N, Nonaka I, Laing NG: Muscle disease caused by mutations in the skeletal muscle alpha-actin gene (ACTA1). Neuromuscul Disord 2003, 13:519−531
9. Costa CF, Rommelaere H, Waterschoot D, Sethi KK, Nowak KJ, Laing NG, Ampe C, Machesky LM: Myopathy mutations in alpha-skeletal-muscle actin cause a range of molecular defects. J Cell Sci 2004, 117:3367−3377
10. Joureau B, de Winter JM, Conijn S, Bogaards SJP, Kovacevic I, Kalganov A, Persson M, Lindqvist J, Stienen GJM, Irving TC, Ma W, Yuen M, Clarke NF, Rassier DE, Malfatti E, Romero NB, Beggs AH, Ottenheijm CAC: Dysfunctional sarcomere contractility contributes to muscle weakness in ACTA1-related nemaline myopathy (NEM3). Ann Neurol 2018, 83:269−282
11. Nguyen MA, Joya JE, Kee AJ, Domazetovska A, Yang N, Hook JW, Lemckert FA, Kettle E, Valova VA, Robinson PJ, North KN, Gunning PW, Mitchell CA, Hardeman EC: Hypertrophy and dietary

tyrosine ameliorate the phenotypes of a mouse model of severe nemaline myopathy. Brain 2011, 134:3516–3529
12. Ravenscroft G, Jackaman C, Bringans S, Papadimitriou JM, Griffiths LM, McNamara E, Bakker AJ, Davies KE, Laing NG, Nowak KJ: Mouse models of dominant ACTA1 disease recapitulate human disease and provide insight into therapies. Brain 2011, 134: 1101–1115
13. Nowak KJ, Wattanasirichaigoon D, Goebel HH, Wilce M, Pelin K, Donner K, Jacob RL, Hubner C, Oexle K, Anderson JR, Verity CM, North KN, Iannaccone ST, Muller CR, Nurnberg P, Muntoni F, Sewry C, Hughes I, Sutphen R, Lacson AG, Swoboda KJ, Vigneron J, Wallgren-Pettersson C, Beggs AH, Laing NG: Mutations in the skeletal muscle alpha-actin gene in patients with actin myopathy and nemaline myopathy. Nat Genet 1999, 23:208–212
14. Chan C, Fan J, Messer AE, Marston SB, Iwamoto H, Ochala J: Myopathy-inducing mutation H40Y in ACTA1 hampers actin filament structure and function. Biochim Biophys Acta 2016, 1862:1453–1458
15. Tinklenberg J, Meng H, Yang L, Liu F, Hoffmann RG, Dasgupta M, Allen KP, Beggs AH, Hardeman EC, Pearsall RS, Fitts RH, Lawlor MW: Treatment with ActRIIB-mFc produces myofiber growth and improves lifespan in the Acta1 H40Y murine model of nemaline myopathy. Am J Pathol 2016, 186:1568–1581
16. Fan J, Chan C, McNamara EL, Nowak KJ, Iwamoto H, Ochala J: Molecular consequences of the myopathy-related d286g mutation on actin function. Front Physiol 2018, 9:1756
17. Tinklenberg JA, Siebers EM, Beatka MJ, Meng H, Yang L, Zhang Z, Ross JA, Ochala J, Morris C, Owens JM, Laing NG, Nowak KJ, Lawlor MW: Myostatin inhibition using mRK35 produces skeletal muscle growth and tubular aggregate formation in wild type and TgACTA1D286G nemaline myopathy mice. Hum Mol Genet 2018, 27:638–648
18. Slick RA, Tinklenberg JA, Sutton J, Zhang L, Meng H, Beatka MJ, Vanden Avond M, Prom MJ, Ott E, Montanaro F, Heisner J, Toro R, Granzier H, Geurts AM, Stowe DF, Hill RB, Lawlor MW: Aberrations in energetic metabolism and stress-related pathways contribute to pathophysiology in the Neb conditional knockout mouse model of nemaline myopathy. Am J Pathol 2023, 193:1528–1547
19. Tinklenberg JA, Siebers EM, Beatka MJ, Fickau BA, Ayres S, Meng H, Yang L, Simpson P, Granzier HL, Lawlor MW: Myostatin inhibition using ActRIIB-mFc does not produce weight gain or strength in the nebulin conditional KO mouse. J Neuropathol Exp Neurol 2019, 78:130–139
20. Meng H, Janssen PM, Grange RW, Yang L, Beggs AH, Swanson LC, Cossette SA, Frase A, Childers MK, Granzier H, Gussoni E, Lawlor MW: Tissue triage and freezing for models of skeletal muscle disease. J Vis Exp 2014:51586
21. Wang H, Marrosu E, Brayson D, Wasala NB, Johnson EK, Scott CS, Yue Y, Hau KL, Trask AJ, Froehner SC, Adams ME, Zhang L, Duan D, Montanaro F: Proteomic analysis identifies key differences in the cardiac interactomes of dystrophin and micro-dystrophin. Hum Mol Genet 2021, 30:1321–1336
22. Bourdon A, Francois V, Zhang L, Lafoux A, Fraysse B, Toumaniantz G, Larcher T, Girard T, Ledevin M, Lebreton C, Hivonnait A, Creismeas A, Allais M, Marie B, Guguin J, Blouin V, Remy S, Anegon I, Huchet C, Malerba A, Kao B, Le Heron A, Moullier P, Dickson G, Popplewell L, Adjali O, Montanaro F, Le Guiner C: Evaluation of the dystrophin carboxy-terminal domain for micro-dystrophin gene therapy in cardiac and skeletal muscles in the DMD(mdx) rat model. Gene Ther 2022, 29:520–535
23. Keller A, Nesvizhskii AI, Kolker E, Aebersold R: Empirical statistical model to estimate the accuracy of peptide identifications made by MS/MS and database search. Anal Chem 2002, 74:5383–5392
24. Liu H, Sadygov RG, Yates JR 3rd: A model for random sampling and estimation of relative protein abundance in shotgun proteomics. Anal Chem 2004, 76:4193–4201
25. Lawlor MW, Viola MG, Meng H, Edelstein RV, Liu F, Yan K, Luna EJ, Lerch-Gaggl A, Hoffmann RG, Pierson CR, Buj-Bello A, Lachey JL, Pearsall S, Yang L, Hillard CJ, Beggs AH: Differential muscle hypertrophy is associated with satellite cell numbers and Akt pathway activation following activin type IIB receptor inhibition in Mtm1 p.R69C mice. Am J Pathol 2014, 184:1831–1842
26. Schneider CA, Rasband WS, Eliceiri KW: NIH Image to ImageJ: 25 years of image analysis. Nat Methods 2012, 9:671–675
27. Garcia-Cazarin ML, Snider NN, Andrade FH: Mitochondrial isolation from skeletal muscle. J Vis Exp 2011:2452
28. Sivandzade F, Bhalerao A, Cucullo L: Analysis of the mitochondrial membrane potential using the cationic JC-1 dye as a sensitive fluorescent probe. Bio Protoc 2019, 9:e3128
29. Perez-Riverol Y, Bai J, Bandla C, Garcia-Seisdedos D, Hewapathirana S, Kamatchinathan S, Kundu DJ, Prakash A, Frericks-Zipper A, Eisenacher M, Walzer M, Wang S, Brazma A, Vizcaino JA: The PRIDE database resources in 2022: a hub for mass spectrometry-based proteomics evidences. Nucleic Acids Res 2022, 50:D543–D552
30. Lamon S, Wallace MA, Russell AP: The STARS signaling pathway: a key regulator of skeletal muscle function. Pflueg Arch Eur J Physiol 2014, 466:1659–1671
31. Zaborske JM, Narasimhan J, Jiang L, Wek SA, Dittmar KA, Freimoser F, Pan T, Wek RC: Genome-wide analysis of tRNA charging and activation of the eIF2 kinase Gcn2p. J Biol Chem 2009, 284:25254–25267
32. Brand MD, Nicholls DG: Assessing mitochondrial dysfunction in cells. Biochem J 2011, 435:297–312
33. Ranu N, Laitila J, Dugdale HF, Mariano J, Kolb JS, Wallgren-Pettersson C, Witting N, Vissing J, Vilchez JJ, Fiorillo C, Zanoteli E, Auranen M, Jokela M, Tasca G, Claeys KG, Voermans NC, Palmio J, Huovinen S, Moggio M, Beck TN, Kontrogianni-Konstantopoulos A, Granzier H, Ochala J: NEB mutations disrupt the super-relaxed state of myosin and remodel the muscle metabolic proteome in nemaline myopathy. Acta Neuropathol Commun 2022, 10:185
34. Tonelli C, Chio IIC, Tuveson DA: Transcriptional regulation by Nrf2. Antioxidants Redox Signal 2018, 29:1727–1745